J. Fluid Mech. (2007), *vol.* 591, *pp.* 255–288.
doi:10.1017/S0022112007008464 Printed in the United Kingdom

Accelerated flow past a symmetric aerofoil: experiments and computations

T. K. SENGUPTA[1], T. T. LIM[2], SHARANAPPA V. SAJJAN[1], S. GANESH[2] AND J. SORIA[3]

[1]Department of Aerospace Engineering, I.I.T. Kanpur, U.P. 208016, India
tksen@iitk.ac.in

[2]Department of Mechanical Engineering, National University of Singapore, Singapore 119260
mpelimtt@nus.edu.sg

[3]Department of Mechanical Engineering, Monash University, Melbourne, VIC 3168, Australia
julio.soria@eng.monash.edu.au

(Received 21 September 2006 and in revised form 22 June 2007)

Accelerated flow past a NACA 0015 aerofoil is investigated experimentally and computationally for Reynolds number $Re = 7968$ at an angle of attack $\alpha = 30^\circ$. Experiments are conducted in a specially designed piston-driven water tunnel capable of producing free-stream velocity with different ramp-type accelerations, and the DPIV technique is used to measure the resulting flow field past the aerofoil. Computations are also performed for other published data on flow past an NACA 0015 aerofoil in the range $5200 \leqslant Re \leqslant 35\,000$, at different angles of attack. One of the motivations is to see if the salient features of the flow captured experimentally can be reproduced numerically. These computations to solve the incompressible Navier–Stokes equation are performed using high-accuracy compact schemes. Load and moment coefficient variations with time are obtained by solving the Poisson equation for the total pressure in the flow field. Results have also been analysed using the proper orthogonal decomposition technique to understand better the evolving vorticity field and its dependence on Reynolds number and angle of attack. An energy-based stability analysis is performed to understand unsteady flow separation.

1. Introduction

Unsteady viscous flow has been studied experimentally and computationally for a long time owing to its scientific interest and technological applications. In general, unsteady flows are divided into two categories. In the first category, one studies the response of viscous flows to dynamic disturbances and, in the second category, the unsteady fields that are created by background disturbances, amplified and self-sustained, are studied. We are concerned here primarily with the former while the second aspect is known to be automatically introduced at high angles of attack, with or without flow acceleration. A better understanding of unsteady effects is necessary for the prediction and control of such flows. These effects are crucial to aircrafts, helicopters, turbomachineries and other engineering applications as discussed in McCroskey (1982).

Externally driven viscous flow can be divided into two broad classes depending on the changes brought about in their aerodynamic environment:

(i) when a body is moving in oscillating or plunging motion with a prescribed acceleration and

(ii) when a body is held fixed and the oncoming flow is allowed to change. e.g. as in translational acceleration or deceleration.

The case of translational acceleration is important as it relates to the flow establishment process in an experimental facility and in real-time applications, as in aerodynamic decelerators. The acceleration and deceleration process can induce large transient loads, limiting the performance and even leading to failure of the device. In this context, the most studied case is the impulsive start of the body. The reason behind the assumption of impulsive motion is that in many practical applications this is adequate and, furthermore, it results in significant simplifications of the mathematical formulations of the problem and can be used for validation of various numerical methods. Early studies of typical impulsive viscous flow problems are due to Stokes (1851) and Rayleigh (1911) and involved obtaining the solution for an infinite flat plate started impulsively into motion in its own plane. Stuart (1963) and Schlichting (1979) have discussed another class of problems involving the establishment of free-stream speed with uniform acceleration. The problems of the boundary layer over a flat plate and circular cylinder with uniform acceleration were solved initially by Blasius and later extended by Görtler (see Schlichting 1979) for a general class of non-uniform acceleration. Collins & Dennis (1974) and Badr, Dennis & Kocabiyik (1996) have studied the symmetrical flow past accelerated circular cylinders. They obtained analytical and computational solutions of the Navier–Stokes equations in the boundary layer coordinates using a perturbation series technique.

In numerical computations one often makes an implicit assumption that the long-time dynamics of the flow is independent of the initial start-up process. In Gendrich, Koochesfahani & Visbal (1995) and Koochesfahani & Smiljanovski (1993) it has been shown that for a dynamically pitching aerofoil, the load and surface pressure distribution on the aerofoil suction surface is affected only for a short time after the end of the initial acceleration period. Lugt & Haussling (1978) have studied the effect of acceleration on an ellipse of thickness to chord ratio (t/c) of 0.1 and concluded that after the acceleration phase is over, differences in the flow characteristics among various types of accelerations vanish rapidly. However, it should be noted that in both Gendrich *et al.* (1995) and Lugt & Haussling (1978), the acceleration ended before leading-edge separation began. Sarpkaya (1991) has studied the effect of uniform acceleration for flow past a circular cylinder. He defined a non-dimensional acceleration parameter A_p given by

$$A_p = D\frac{\mathrm{d}U_\infty}{\mathrm{d}t}\Big/\bar{U}_\infty^2$$

where D is the cylinder diameter, $\bar{U}_\infty$ is the final velocity and U_∞ is the instantaneous velocity. He noted that for $A_p > 0.27$, the drag coefficient beyond the period of initial acceleration does not measurably depend on A_p and the flow can be considered as impulsively started. The drag overshoot and the relative displacement of the cylinder to reach this value remain more or less the same. For $A_p < 0.27$, the drag overshoot reduces to its commonly accepted quasi-steady value as soon as the acceleration is removed. However, Sarpkaya (1991) could not get repeatability of lift force for his experiments and stated that the lift force depends on initial disturbances that were not maintainable during different experimental runs. Furthermore, he argued on the basis of his experimental results that the manner in which acceleration is removed from the flow to sustain a constant velocity turned out to be more important than

the manner in which the acceleration is imposed. For a dynamically pitching aerofoil, Choudhuri & Knight (1996), Currier & Fung (1992) and Carr & Chandrasekhara (1996) have noted that the compressibility is one of the major parameters affecting the flow. For the translational accelerations studied here, compressibility does not play a major role, as noted by comparing the peak suction values for the present cases to the results of Currier & Fung (1992). In the present work, we concentrate on the effects of translational flow acceleration at low Reynolds numbers for incompressible flow past aerofoils at high angles of attack.

One of the earliest computational works on the starting solution for flow past an aerofoil is by Mehta & Lavan (1975) who studied the problem of laminar flow past an impulsively started 9 % thick Joukowski aerofoil at $Re = 1000$. The flow past the aerofoil was seen to be dominated by the formation, growth and breakup of separation bubbles at this Reynolds number. Depending on the Reynolds number and angle of attack, the unsteady separated flow may undergo laminar to turbulent transition to form long or short bubbles. Whereas the short bubbles have only a small effect on the pressure distribution, the long bubbles result in a pressure distribution that is different from the inviscid value. Ohmi *et al.* (1991) have presented some experimental and computational results for a NACA 0012 aerofoil at 30° angle of attack for $Re = 3000$. Nair & Sengupta (1998) have presented results for initial times with different start-up processes. Morikawa & Grönig (1995) have studied, experimentally and computationally, the unsteady aerodynamics of a NACA 0015 aerofoil and provided a record of tunnel free-stream speed as a function of time for the starting process. In the present study, we compute and compare with this experimental result for uniform flow past a NACA 0015 aerofoil at an angle of attack of 30° for $Re = 35\,000$ for the given time history of the free-stream speed. A tangent hyperbolic representation was closest to the measured speed distribution in Morikawa & Grönig (1995) and is given by

$$U_\infty(t) = \bar{U}_\infty \tanh\left(\frac{t^*}{\tau^*}\right) \tag{1.1}$$

with $\bar{U}_\infty$ the final steady tunnel speed and $\tau^* = 50\,\text{ms}$, as given in the reference. All calculations reported here are performed with times non-dimensionalized by the convection time scale, constructed from $\bar{U}_\infty$ and the chord of the aerofoil, and are represented by quantities without asterisks. For the numerical procedure followed in Morikawa & Grönig (1995), acceleration of the mean flow was accounted for by an additional source term in the x-momentum equation derived from the time derivative of (1.1). In an earlier experimental work, Freymuth (1985) studied the effect of uniform acceleration on flow past a NACA 0015 aerofoil at different Reynolds numbers and angles of attack by flow visualization. Note that in that work, the Reynolds number was defined in terms of the uniform acceleration and the chord of the aerofoil. His results are reported for Reynolds number held constant, and thus by our convention the Reynolds number based on instantaneous convection speed will vary linearly with time.

Here, we investigate constant acceleration cases (ramp-start) as shown in figure 3 below. Zaman, McKinzie & Rumsey (1989) have shown, based on their experimental results, that the flow past aerofoils near stall can be two-dimensional. This is also supported in Lin & Pauley (1996), Huang & Lin (1995) and Brendal & Mueller (1988) for results obtained at early times after the flow start-up. In the present investigation, our focus is mainly on the flow onset process and the results obtained from the

solution of two-dimensional Navier–Stokes equation are considered adequate. For flow over aerofoils near stall at high Reynolds numbers, the unsteadiness is largely due to the low-frequency events of shed vortices and their convection.

A stream function–vorticity formulation is preferred for the computations here because the smaller number of unknowns compared to using primitive variables makes higher resolution calculations possible. Also, this formulation ensures exact satisfaction of mass conservation, making a smaller demand on computational requirements than needed in the primitive variable formulation. Furthermore, a higher accuracy is achieved by using compact schemes as developed and used in Sengupta (2004) and Sengupta, Vikas & Johri (2005) for the discretization of nonlinear convection terms of the vorticity transport equation. An orthogonal numerical grid generation technique developed in Nair & Sengupta (1998) is used here, which helps to further reduce numerical error. In that work, some comparisons are made with the results of Morikawa & Grönig (1995) for flow past a NACA 0015 aerofoil at a Reynolds number of 35 000 and 30° angle of attack. The calculation was performed using the same formulation, but with a third-order upwinding scheme.

In the present work, we further investigate the constant acceleration case experimentally for $Re = 7968$ and $\alpha = 30^\circ$ for different acceleration parameters, and the details are given in § 2. In § 3, the formulation and the numerical methods used for the computations are given. The following cases are studied here, when flow accelerates from zero velocity at $t = 0$:

A. A uniform acceleration case with $Re = 7968$, $\alpha = 30^\circ$ and $\tau = 3.75$ for which the experimental results are provided in § 2.

B. A uniform flow with a tangent hyperbolic dependence of free-stream speed on time for $Re = 35\,000$, $\alpha = 30^\circ$ and $\tau = 0.6$. This case corresponds to the experiments of Morikawa & Grönig (1995).

C. A uniform flow using a ramp start for $Re = 35\,000$, $\alpha = 30^\circ$ and $\tau = 0.5$ to compare with the case B.

D. A uniform acceleration for $Re = 5\,200$, $\alpha = 60^\circ$ and 90° with very large τ. This corresponds to the experiments of Freymuth (1985). The definition of the Reynolds number for this case is given in § 4.3.

In § 4, computational and various experimental results are discussed case by case. In § 5, proper orthogonal decomposition of two cases is presented for different angles of attack and Reynolds number to distinguish the flow structures at high angles of attack. The paper concludes with a summary in § 6.

2. Experimental setup and procedures

The experiments were conducted in a piston-driven closed-circuit water tunnel in the Fluid Mechanics Laboratory of the National University of Singapore. A schematic drawing of the tunnel is presented in figure 1. Unlike the conventional water tunnel with a continuous flow, this tunnel is driven by a square Plexiglas piston of 198 mm × 198 mm, which pushes the water ahead of it as it slides along the test section with the same dimensions. The piston is driven by a micro-stepper motor (Sanyo Denki, Model 103-8960-0140) via a ball and screw mechanism, which converts the rotational motion into a linear motion of the piston. The motor, which is powered by a micro-steps driver (2D88M) and controlled by TTL signals generated by a Labview Program in a PC, can achieve 10 000 micro-steps per revolution or 0.036° per step. With a pitch of the ball-screw of 25 mm, this translates into a linear resolution of 3.125×10^{-4} mm per step. For safety reasons, the piston is confined to move between

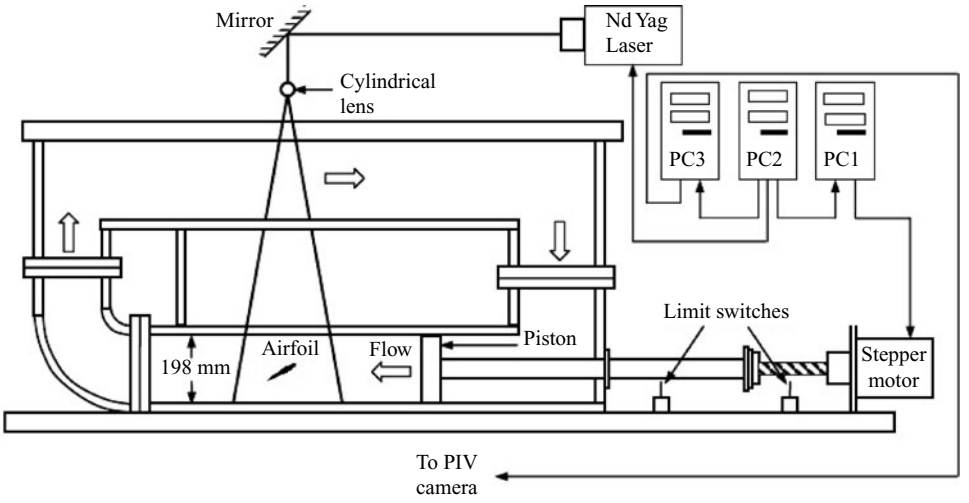

FIGURE 1. A schematic drawing of the experimental set up.

the two limit switches indicated in figure 1 and has a maximum traversing distance of 350 mm. A unique feature of this facility is its ability to execute any predetermined piston motion including that of a power-law: $U_\infty = at^m$, where U_∞ = piston/free-stream velocity, t = elapsed time and, a and m are predetermined constants.

The NACA 0015 aerofoil used in the present investigation has a chord length (c) of 80 mm and spanned the width of the test section giving an aspect ratio (width/chord) of 2.475. The aerofoil was mounted about its quarter-chord point in the middle of the test section using a rotational mechanism, which allows any predetermined angle of attack to be set from outside the water tunnel. To minimize the effect of the corner vortex generated between a moving piston and a stationary wall, the minimum distance between the piston and the model support is kept at 350 mm (or 4.38c).

To conduct particle image velocimetry (PIV) measurements, a continuum Nd:YAG twin cavity laser system capable of delivering 2×300 mJ pulses of 6 ns duration at 10 Hz was used as the illumination source. It was found that operating the laser at frequencies other than 10 Hz would lead to significant deterioration in beam quality. A cylindrical lens was used to expand the laser beam into a thin sheet of 2 mm thickness before it was directed along the centreline of the test section bisecting the test model.

Since the experiments were conducted in an air-conditioned room with a temperature of 23 °C, the water in the tunnel had to be left overnight to attain the room temperature. Dantec polyamide particles with a nominal diameter of 20 μm and a density of $1000 \pm 30\,\mathrm{kg\,m^{-3}}$ were used to seed the flow. The particles were prepared according to the technique described in Soria *et al.* (2003) so that any particles with specific gravity greater or less than one were discarded.

A PCO Pixelfly digital CCD camera with an array of 1280×1024 pixels was used to record PIV images using a double-shutter mode. A 105 mm Micro-Nikkor lens set at an aperture of $f2.8$ and a reproduction ratio of 10.24 was used for all the investigations reported here. Since the laser illumination operated optimally at 10 Hz, the recordings had to be carried out in 100 ms or integral multiple time intervals t_p of it (see figure 2). Here, t_p was fixed at 200 ms which corresponds to the acquisition rate of 5 image pairs per second. The time interval (Δt) between the two laser pulses A and

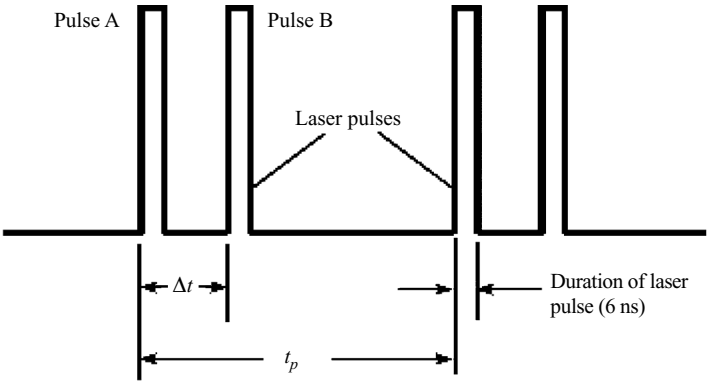

FIGURE 2. Temporal parameters for the laser.

B was determined based on the maximum free-stream velocity. Due to the restriction on the laser operating frequency of 10 Hz, the number of captured PIV images for each flow condition depended on the velocity profile, the maximum velocity and the displacement of the piston.

To ensure correct synchronization of the operation of the piston tank, the laser and the PIV camera, a master control PC2 was used (figure 1). Prior to the experiment, PC1 and PC3, which control the operation of the laser and the motor, respectively were set to 'Slave mode' or 'External triggering mode'. Both the PCs waited for the triggering TTL signal from PC1 before activating their respective devices. All communications between PCs were via an Ethernet cable interface.

The multigrid cross-correlation digital PIV (MCCDPIV) algorithm used to process the raw PIV images is the same as used in Soria *et al.* (2003). Detailed discussion of the data analysis and experimental uncertainty can be found in Soria *et al.* (2003) and is not repeated here. Briefly, a Gaussian function estimator is used for calculating the location of the cross-correlation peak. The interrogation area (IA) was 32×32 pixels with 50 % overlap, and the maximum displacement of the flow field was ensured to be less than 20 % of the IA. All the output files were in Tecplot-readable format.

The experiments described here are for the aerofoil fixed at $\alpha = 30^\circ$ and the oncoming flow subjected to a predetermined linear accelerations from rest of 33.33, 50 and $100\,\mathrm{mm\,s^{-2}}$. Figure 3 shows the corresponding velocity profiles used and the locations of the discrete symbols indicate the instants at which PIV measurements were taken. In all cases, the maximum free-stream velocity (U_∞^*) was $100\,\mathrm{mm\,s^{-1}}$ giving a maximum Reynolds number ($U_\infty c/\nu$) of 7968, where ν is the kinematic viscosity of water.

The opacity of the aerofoil prevented laser illumination below it, and thus this region is excluded from the MCCDPIV analysis here. Also, each realization was repeated 50 times for subsequent ensemble-averaging.

In figure 4, the ensemble-averaged velocity fields are shown for the indicated acceleration rates. In each of the cases, results are shown till the time when $U_\infty(t^*)$ reaches a value of $100\,\mathrm{mm\,s^{-1}}$. It is clearly evident that the formation of separation bubbles and their evolution depends upon the length of time the acceleration is applied and not upon the strength of the acceleration, a point that was mentioned in Sarpkaya (1991) and will also be verified by our calculations. However, at the same non-dimensional times the separation effects are accentuated for the higher acceleration case, as can be seen at $t = 1.5$ for cases (a) and (b). In figure 5, the ensemble-averaged vorticity distributions are shown for the same three acceleration

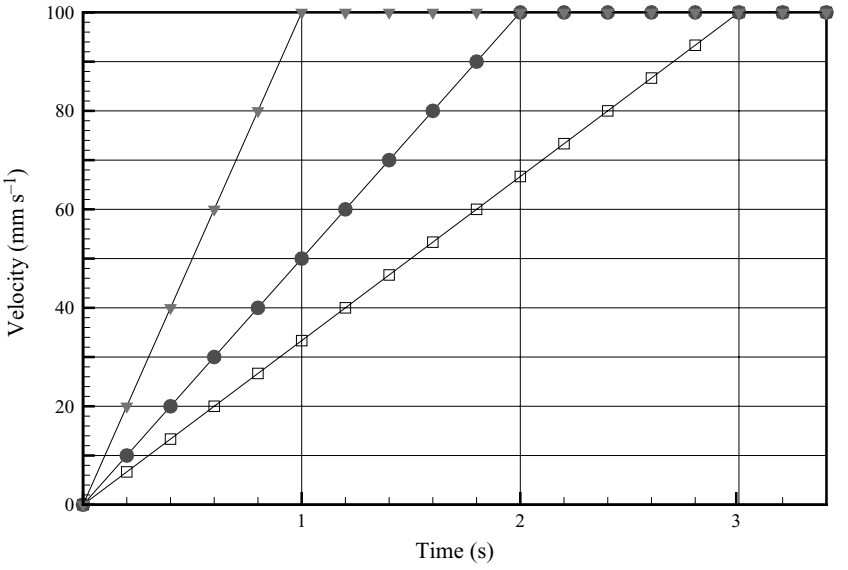

FIGURE 3. Imposed piston velocity profiles for accelerations: $a = 33.33\,\text{mm s}^{-2}$ (open rectangle), $a = 50\,\text{mm s}^{-2}$ (filled circle), $a = 100\,\text{mm s}^{-2}$ and (filled triangle) and constant acceleration of $a = 100\,\text{mm s}^{-2}$ followed by a constant velocity at $100\,\text{mm s}^{-1}$ (open circle).

cases. Here, one can see the effects of the time of application of acceleration on the separation, compared to the effect of the strength of the acceleration. Thus, from figures 4 and 5 it is seen that the maximum effect of acceleration is noted for the case of A33 with $33.33\,\text{mm s}^{-2}$. Corresponding computations for this case are presented below.

3. Computational formulation and methods

Here, unsteady two-dimensional Navier–Stokes equations are solved in terms of stream function and vorticity to study the effects of acceleration on flow past an aerofoil at high angles of attack at moderate Reynolds numbers. The formulation and auxiliary conditions are presented next.

3.1. *The governing equation and formulation*

The unsteady Navier–Stokes equations for incompressible two-dimensional flows in stream function and vorticity formulation are

$$\nabla^2 \boldsymbol{\psi} = -\boldsymbol{\omega}, \tag{3.1}$$

$$\frac{\partial \boldsymbol{\omega}}{\partial t} + \nabla \cdot (\boldsymbol{\omega} \boldsymbol{V}) = \frac{1}{Re} \nabla^2 \boldsymbol{\omega}, \tag{3.2}$$

where the stream function is related to the velocity field by

$$\boldsymbol{V} = \nabla \times \boldsymbol{\psi}. \tag{3.3}$$

The only non-zero component of vorticity for the two-dimensional flow is given by

$$\boldsymbol{\omega} = |\nabla \times \boldsymbol{V}| \boldsymbol{k}. \tag{3.4}$$

Unless stated otherwise, all lengths are non-dimensionalized with respect to the chord of the aerofoil and the velocities by the final free-stream speed ($\bar{U}_\infty$).

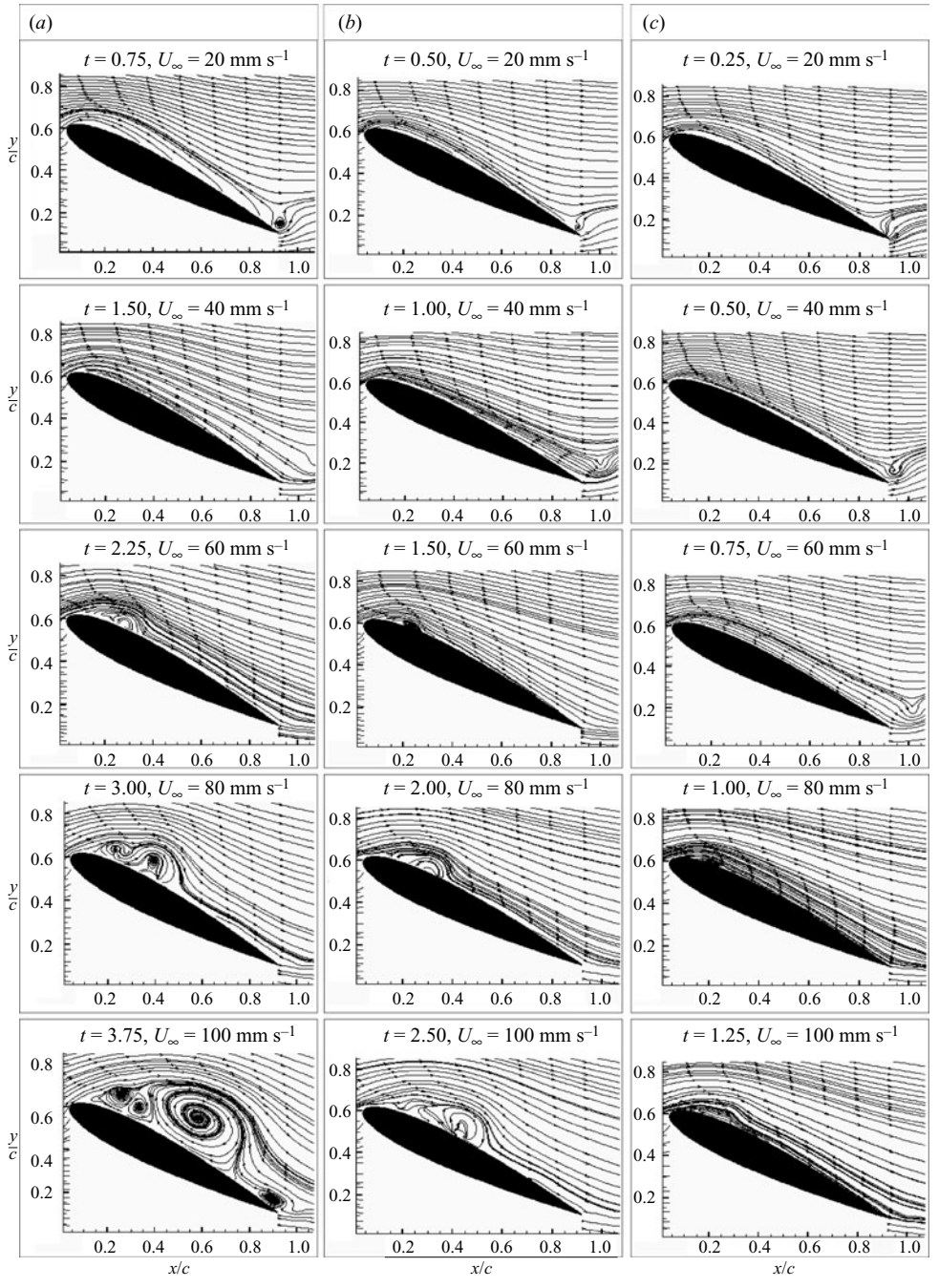

FIGURE 4. Ensemble-averaged velocity fields for three different accelerations. Time increases from top to bottom, and acceleration increases from left to right. (*a*) $a = 33.33\,\mathrm{mm\,s^{-2}}$, (*b*) $a = 50\,\mathrm{mm\,s^{-2}}$, (*c*) $a = 100\,\mathrm{mm\,s^{-2}}$. $t = t^* U_\infty^* / c$ represents the non-dimensional time.

Equations (3.1) and (3.2) are solved in the transformed plane obtained by a numerically generated O-grid following the methodology of Nair & Sengupta (1998). The governing stream function equation and vorticity transport equation are given in

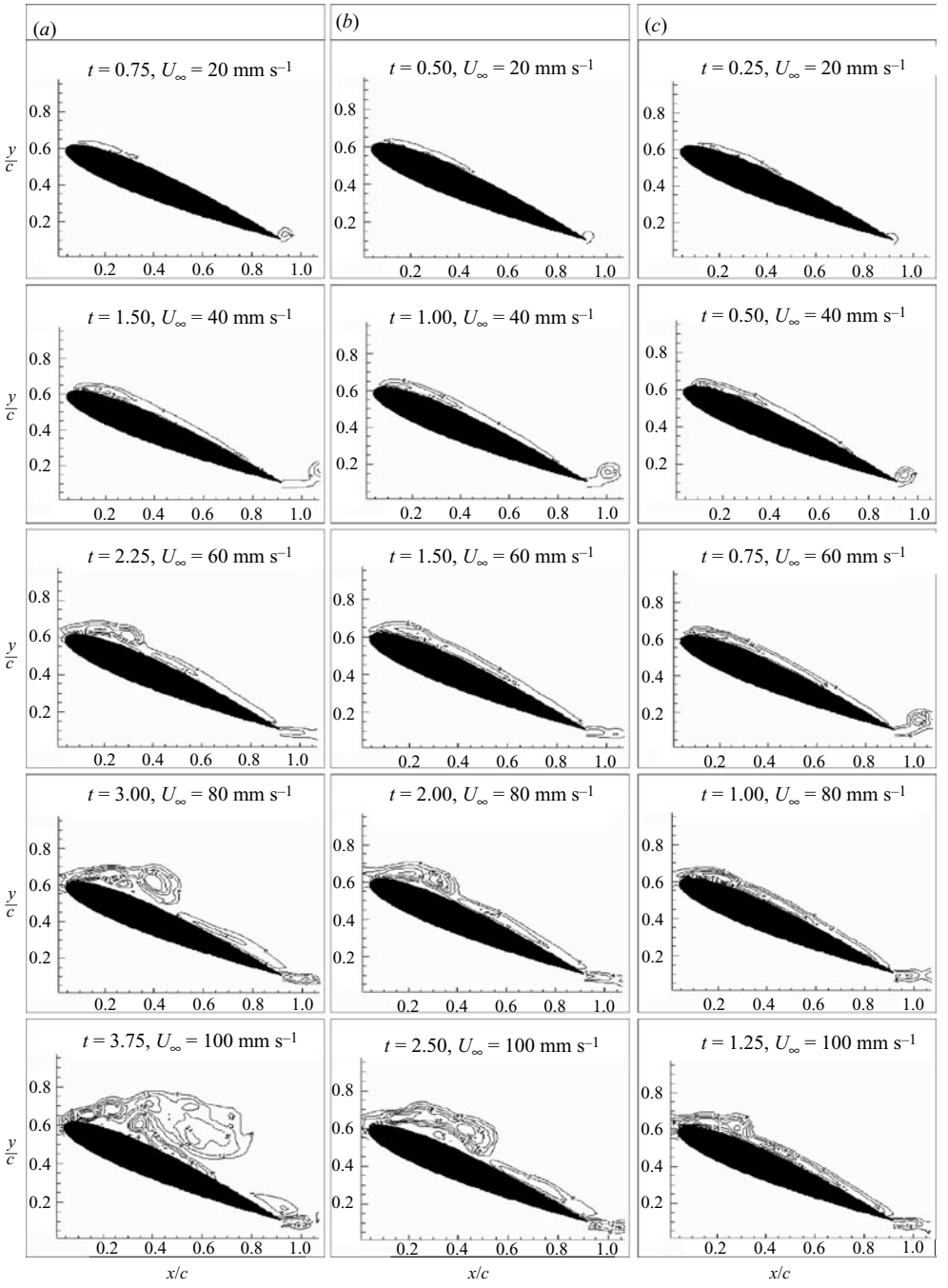

FIGURE 5. Ensemble-averaged vorticity contour plots for three different accelerations. Time increases from top to bottom, and acceleration increases from left to right. (*a*) $a = 33.33\,\mathrm{mm\,s^{-2}}$, (*b*) $a = 50\,\mathrm{mm\,s^{2}}$, (*c*) $a = 100\,\mathrm{mm\,s^{-2}}$. $t = t^* U_\infty^*/c$ represents the non-dimensional time.

the transformed (ξ, η)-plane by

$$\frac{\partial}{\partial \xi}\left[\frac{h_2}{h_1}\frac{\partial \psi}{\partial \xi}\right] + \frac{\partial}{\partial \eta}\left[\frac{h_1}{h_2}\frac{\partial \psi}{\partial \eta}\right] = -h_1 h_2 \omega, \tag{3.5}$$

$$h_1 h_2 \frac{\partial \omega}{\partial t} + h_2 u \frac{\partial \omega}{\partial \xi} + h_1 v \frac{\partial \omega}{\partial \eta} = \frac{1}{Re}\left[\frac{\partial}{\partial \xi}\left(\frac{h_2}{h_1}\frac{\partial \omega}{\partial \xi}\right) + \frac{\partial}{\partial \eta}\left(\frac{h_1}{h_2}\frac{\partial \omega}{\partial \eta}\right)\right], \tag{3.6}$$

where h_1 and h_2 are scale factors of the transformation, given by $h_1^2 = (x_\xi^2 + y_\xi^2)$ and $h_2^2 = (x_\eta^2 + y_\eta^2)$.

In the transformed plane, the components of velocity are,

$$u = \frac{1}{h_2}\frac{\partial \psi}{\partial \eta}, \qquad v = -\frac{1}{h_1}\frac{\partial \psi}{\partial \xi}. \tag{3.7}$$

The stream function–vorticity formulation provides higher accuracy with respect to incompressibility assumption, but it does not yield the pressure field. Currier & Fung (1992) and Ramiz & Acharya (1992) have used experimental pressure coefficients to study unsteady separation. There is a need to accurately evaluate the pressure field better to understand unsteady flows since pressure fluctuations contain the signature of coherent vortices located at the pressure trough. It has also been noted by Lesieur & Metais (1996) that low-pressure regions are better indicators of the coherent vortices than the high vorticity regions.

Thus, we solve the Poisson equation for the total pressure to obtain the pressure field over the full computational domain. The governing Poisson equation for pressure is obtained by taking the divergence of the Navier–Stokes equation in primitive variables. For an orthogonal curvilinear coordinate system, this is

$$\frac{\partial}{\partial \xi}\left(\frac{h_2}{h_1}\frac{\partial P}{\partial \xi}\right) + \frac{\partial}{\partial \eta}\left(\frac{h_1}{h_2}\frac{\partial P}{\partial \eta}\right) = \frac{\partial}{\partial \xi}(h_2 v\omega) - \frac{\partial}{\partial \eta}(h_1 u\omega). \tag{3.8}$$

This formulation in an orthogonal grid was used earlier in Nair & Sengupta (1997*a*), which can be consulted for further details. The physical and computational domains for the present investigation are shown in figure 6(*a*). The numerically obtained orthogonal grid is shown in figure 6(*b*). Note that a similar calculation for the effect of acceleration was reported in Nair & Sengupta (1997*b*), where a third-order upwind scheme (as given in Nair & Sengupta 1997*a*) was used with similar grids. In Sengupta *et al.* (2006), the same formulation has been used for flow past an aerofoil executing flapping and hovering motion using compact schemes. It is well known that compact schemes provide much higher resolution than explicit higher-order upwind schemes, thus enabling us to obtain numerical solutions with significantly enhanced accuracy.

3.2. *Initial and boundary conditions*

On the solid boundary ABC (in figure 6) the no-slip conditions apply,

$$\psi = \text{constant}, \quad \frac{\partial \psi}{\partial \eta} = 0. \tag{3.9}$$

These conditions also fix the wall vorticity, which is required as the boundary condition for the vorticity transport equation. Periodic boundary conditions are applied at the cuts (AF and CD) for all variables. For the stream function equation, at the outer boundary the Neumann boundary condition is used: $\partial \psi/\partial \eta = U_\infty \partial y/\partial \eta$. To solve the vorticity transport equation, a fully developed condition is used as the boundary condition: $\partial \omega/\partial \eta = 0$. From equation (3.5), wall vorticity is calculated as

$$\omega|_{body} = -\frac{1}{h_2^2}\frac{\partial^2 \psi}{\partial \eta^2}\bigg|_{body}. \tag{3.10}$$

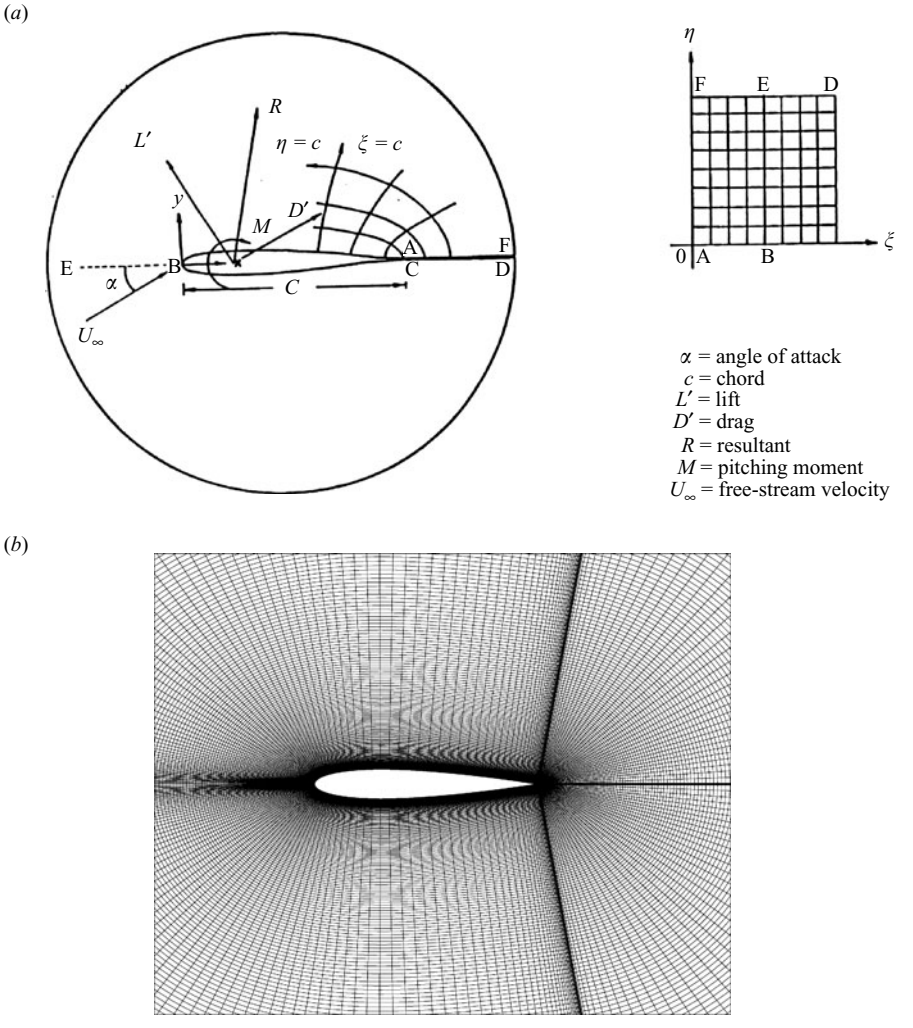

FIGURE 6. (*a*) Physical and computational domain and (*b*) the (257 × 301) grids used for the NACA 0015 aerofoil. Only a close-up of the grid is shown.

For the Poisson equation (3.8), the Neumann boundary condition as obtained from the normal (η)-momentum equation is used on the surface and the outer boundary, whereas the periodic boundary condition applies at the cuts.

3.3. *Numerical method*

The numerical method used here is well-tested and has already been used in Sengupta, Ganeriwal & De (2003) and Sengupta *et al.* (2006). The finite difference form of various derivatives in (3.5) and (3.6) is obtained by employing central differencing, except the convection terms of (3.6), which has been discretized using high-accuracy compact schemes outlined in Sengupta *et al.* (2003). In compact schemes, a general recursion relation of the following form is used to evaluate first derivatives (indicated by primed quantities):

$$b_{j-1}u'_{j-1} + b_j u'_j + b_{j+1}u'_{j+1} = \frac{1}{h}\sum_{k=-2}^{2} a_{j+k}u_{j+k}. \tag{3.11}$$

In the periodic ξ-direction, the truncation error is minimized in the least-squares sense, by choosing the following coefficients in the above equation: $b_{j\pm1} = 0.3793894912$, $b_j = 1$, $a_{j\pm1} = \pm 0.7877868$, $a_{j\pm2} = \pm 0.0458012$ and $a_j = 0$. The periodic tridiagonal system obtained by the application of (3.11) for different nodes is solved to evaluate the required ξ-derivatives in this direction.

In the non-periodic η-direction, one cannot apply the stencil (3.11) for all the nodes. For example, stable boundary closure schemes are required for the first and second node. The ones used are given by

$$u_1' = \frac{(-3u_1 + 4u_2 - u_3)}{2h}, \tag{3.12}$$

$$u_2' = \left[\left(\frac{2\beta_2}{3} - \frac{1}{3}\right)u_1 - \left(\frac{8\beta_2}{3} + \frac{1}{2}\right)u_2 + (4\beta_2 + 1)u_3 - \left(\frac{8\beta_2}{3} + \frac{1}{6}\right)u_4 + \frac{2\beta_2}{3}u_5\right] \Big/ h, \tag{3.13}$$

with β_2 as a parameter to be chosen to ensure accuracy and stability. Similarly, boundary closure schemes are used for $j = (N-1)$ and $j = N$ with another parameter, β_{N-1}. For the boundary closure, we have used $\beta_2 = -0.09$ and $\beta_{N-1} = 0.09$. Application of (3.11) and the boundary closure schemes for different nodes in the η-direction leads to a tridiagonal system that can be solved to obtain the derivatives with respect to η for the vorticity. To numerically stabilize the computations, an explicit fourth dissipation term is added to the calculated first derivatives (see Sengupta *et al.* 2006 for further details).

4. Results and discussion

The orthogonal grids of size (257×301) were generated for the aerofoil by the procedure developed in Nair & Sengupta (1998) and shown in figure 6(*b*), for few representative grid lines close to the aerofoil. The grid generation method is based on the solution of the Beltrami equation, a hyperbolic partial differential equation of order two, in which, starting from the aerofoil surface, constant-η lines are generated by marching outwards with prescribed grid spacing in the hyperbolic direction. This ability to prescribe the spacing in the normal direction is an added advantage of the grid generation method used and helps to provide adequate resolution in the wall-normal direction and in the wake region. Also, the spacing in the normal direction is chosen in such a way that the truncation error does not give rise to spurious dispersion and dissipation. This is one of the important aspects of the present solution methodology. The outer boundary is located 12 chords away from the body. The present orthogonal grid needs fewer terms to be discretized than a non-orthogonal grid, which reduces the sources of truncation error. For the results presented here, a grid spacing of $0.00001c$ was used in the direction normal to the aerofoil surface.

The time integration of VTE uses a time step of $\Delta t = 0.00001$ for the calculations presented. The choice of the time step was dictated by the required accuracy and to avoid numerical instability for the explicit four-stage Runge–Kutta method used. Also, it should be noted that the loads are obtained by the vorticity values and the pressure values on the surface obtained by solving the pressure Poisson equation. One of the advantages of the present method is that the pressure field can be calculated off-line, which increases the speed of the overall computations. As noted earlier, the purpose of the computation is to aid in understanding the effects of different levels and types of acceleration on the growth and shedding of vortices. Before discussing these, it

is necessary to introduce some general terminologies used in this section. A surface bubble is considered closed if it is completely enclosed by the body streamline. Additional closed streamline loops can also be present inside an enclosed bubble, and their centres are different from the centre of the enclosed bubble. Bubbles are defined as clockwise or anticlockwise depending on the direction of the velocity vector associated with the closed streamline inside them. Similarly a vortex is represented by a closed equivorticity line. Perry, Chong & Lim (1982) provide a descriptive understanding of near-wake vortex formation, and have used the term *alleyway* to describe the vortex shedding phenomena by examining instantaneous streamlines. *Alleyway* refers to an instantaneous passage in the near-wake region where the streamlines upstream do not begin or end at critical points (i.e. points where all velocity components are zero).

Some preliminary results were presented by Nair & Sengupta (1997*b*, 1998) and compared their simulations with the corresponding experimental results at different *Re*. For a truly impulsive start, the conditions at $t = 0$ should correspond to that of an inviscid flow. Different types of flow start-up that are studied here are shown in figures 7(*a*) and 7(*b*). In figure 7(*a*), two different approaches to achieve the same final velocity are presented: the first one is that used in Morikawa & Grönig (1995) and given by equation (1.1); the second is the case of a ramp-start that takes the flow from zero to the final velocity by a uniform acceleration. In figure 7(*b*), the piston velocity–time profile used in the present experiment and computation is presented for the A33 case. In the experiments, a constant accelerated start is followed by a constant deceleration, so that the flow velocity is zero after 6 s. In all the experiments, the maximum velocity attained is $100\,\mathrm{mm\,s^{-1}}$ and computations are performed here only for the case $a = 33.33\,\mathrm{mm\,s^{-2}}$. While the velocity shown in figure 7(*b*) corresponds to the piston velocity, we have also measured the actual flow velocity at the centreline of the tunnel, and the velocity–time record is shown in figure 7(*c*). Note that the kinks in the velocity profile in figure 7(*c*) are caused by an uneven expansion of the square Plexiglas piston tank when filled with water. In air, the piston slides smoothly along the walls of the tank, but with water, the uneven absorption of the water by the Plexiglas wall plus the weight of the water distorts the test section slightly from its original square shape. Attempts were made to rectify the problem by trimming the dimension of the piston to match that of the tank, but the size of the piston could not be reduced too much, otherwise the mismatch would cause the flow to leak through the gaps between the piston and the tank. Despite the unavoidable problem, the velocity distribution (in an average sense) still displays a reasonable 'constant' acceleration and deceleration. The occurrence of the kinks equidistant in time is due to the DPIV system which only allows velocity measurements at discrete time intervals. We have performed computations for both the cases depicted in figures 7(*b*) and 7(*c*) and compared them to understand the role of the small variation in acceleration seen in figure 7(*c*). Next we present results for different cases identified at the end of § 1 as Cases A to D.

4.1. *Case A*

In this case, the acceleration of flow from zero to a final velocity of $100\,\mathrm{mm\,s^{-1}}$ was achieved in 3 s via a uniform acceleration, and the corresponding results are shown in figures 4 and 5 (case *a*). Experimentally obtained instantaneous integral curves generated from the instantaneous velocity field are compared with the computed streamline contours obtained up to $t = 3.75$ (non-dimensional time) in figure 8 for the piston velocity–time profile shown in figure 7(*b*). These two sets of results are shown in the first and middle columns of figure 8. Another case is computed using

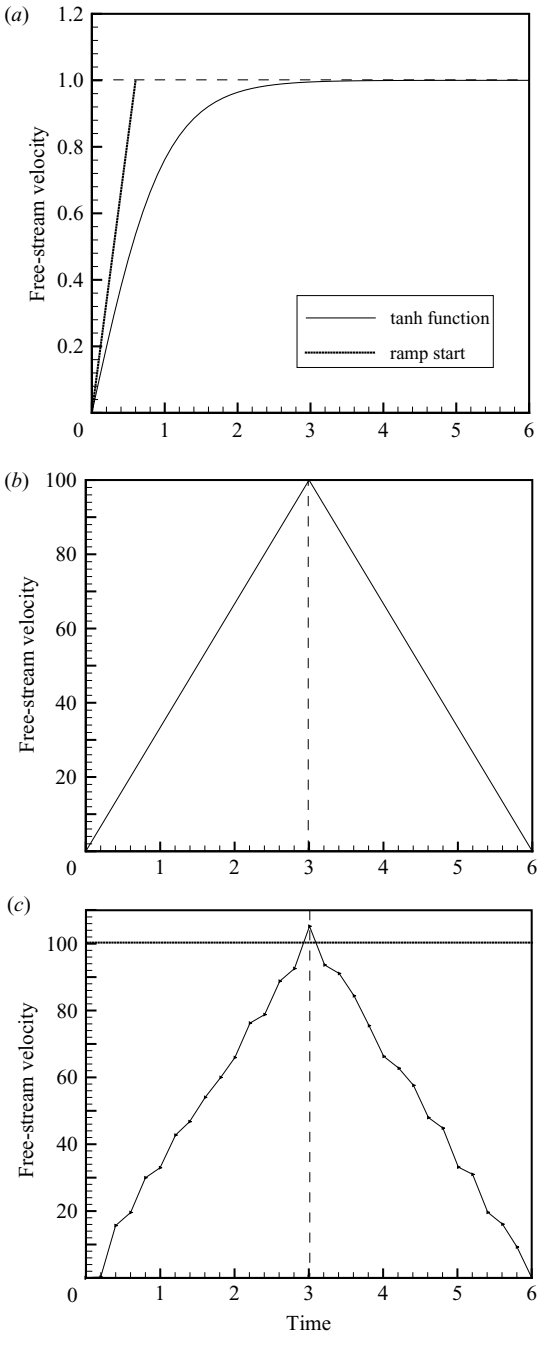

FIGURE 7. (*a*) A sketch of non-dimensional velocity–time profile for a tangent hyperbolic and ramp-start flow. (*b*) Imposed piston velocity–time profile for the experimental results reported in figures 4 and 5. (*c*) Measured velocity–time record at the centreline of the tunnel for the case (*b*).

the measured velocity–time profile depicted in figure 7(*c*). The results for this case are shown in the third column of figure 8. While the experimental results match very well at early times with the computations performed with the piston velocity–time

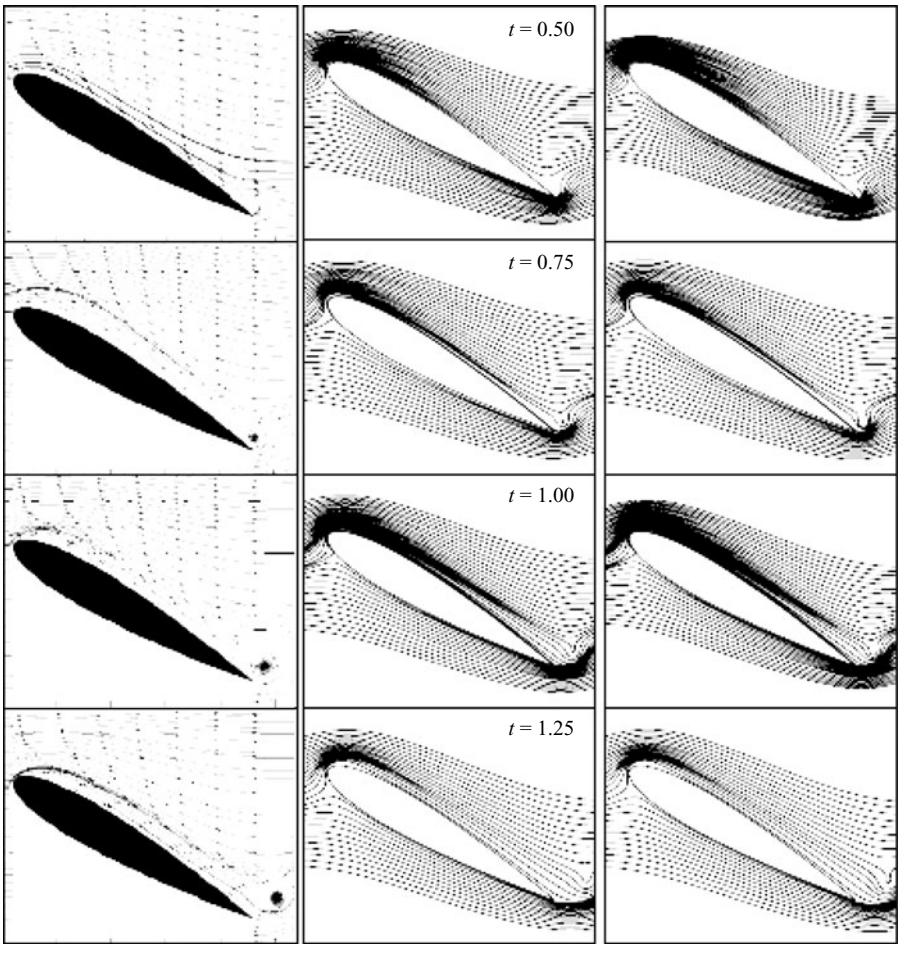

FIGURE 8. For caption see page 271.

record in figure 7(*b*), the starting vortex is seen to be larger than the computed result. This under-estimation in the computation is due to the fact that the calculated wall vorticity at early times is filtered by the numerical differencing procedure. At later times, it is seen that the computation performed using the actual velocity distribution (figure 7*c*) show a better agreement with the experimental data than that computed with the piston velocity–time profile in figure 7(*b*). In figure 9, corresponding computed vorticity contours are plotted and compared with the experimental data shown in the first column. Similar to the streamline contour plots, the computations performed with the actual velocity data show better match with the experimental data, especially at later times, as seen at $t = 3.75$. Thus, it appears that the slight difference in acceleration levels between the actual velocity data and the data from the constant acceleration of the piston velocity leads to some differences in the flow evolution. We should also point out that the actual velocity data are obtained after filtering the high-frequency components and the absence of these components can also account for the residual differences. The velocity data of figure 7(*c*) should be compared with the record shown in figure 2 of Morikawa & Grönig (1995), where the measured free-stream record showed the presence of very high-frequency fluctuations as the

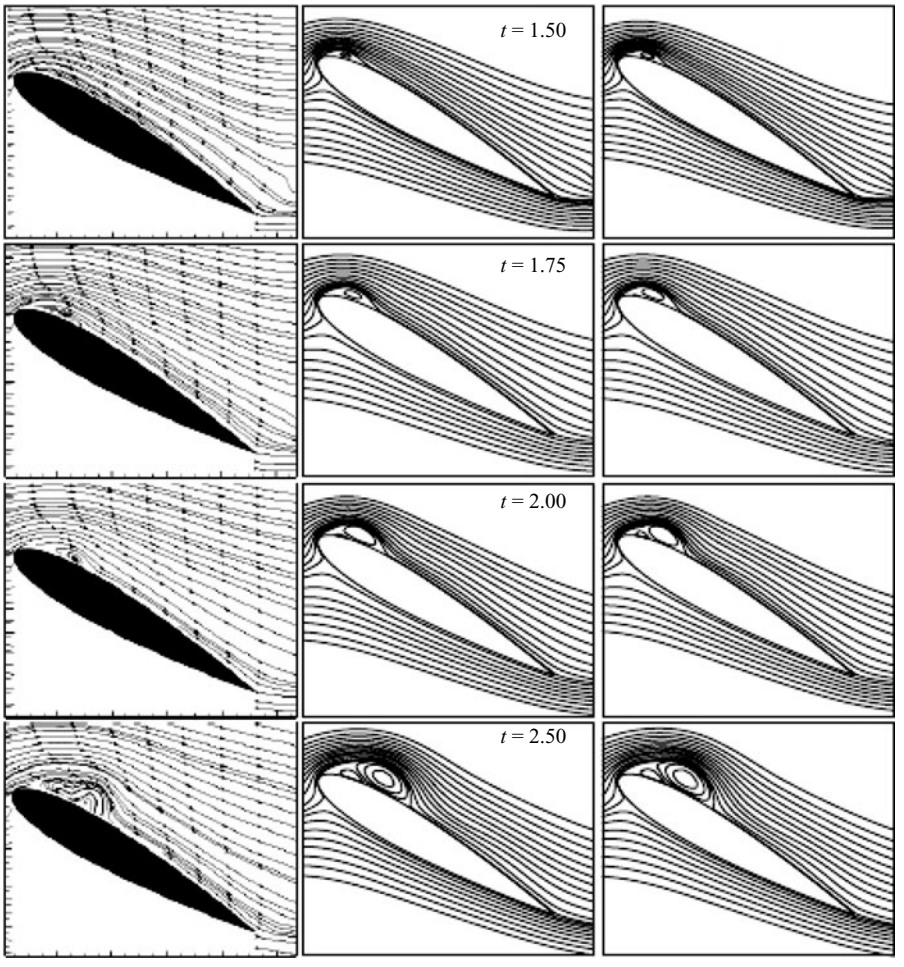

FIGURE 8. For caption see facing page.

flow reached the terminal constant-velocity stage. Since the results shown in figures 8 and 9 correspond to the maximum *Re* of 7968, which is a relatively low value to record the effects of acceleration at $\alpha = 30^\circ$, another case is considered next, where the terminal maximum *Re* is 35 000.

4.2. *Cases B and C*

Case B corresponds to the same free-stream speed as studied experimentally by Morikawa & Grönig (1995) and is given by (1.1). The value of $\tau = 0.6$ corresponds to the physical time of 50 ms that was the dimensional start-up time scale in the experiments. Likewise, the computation is carried out using (1.1) with $\tau = 0.6$. Figure 10 compares the present computation with the results of Morikawa & Grönig (1995) at $t = 2.903$. In figure 10(*a*), the experimental snapshot is shown, while in figure 10(*b*) the computed streamlines are shown, when the free stream is established following equation (1.1). It can be seen that the present computed results match the experimentally visualized streamlines better than the computed results of Morikawa & Grönig (1995) as depicted in figure 10(*c*). Particularly noticeable is the failure of the computed results of figure 10(*c*) to capture the flattened bubble located over the top

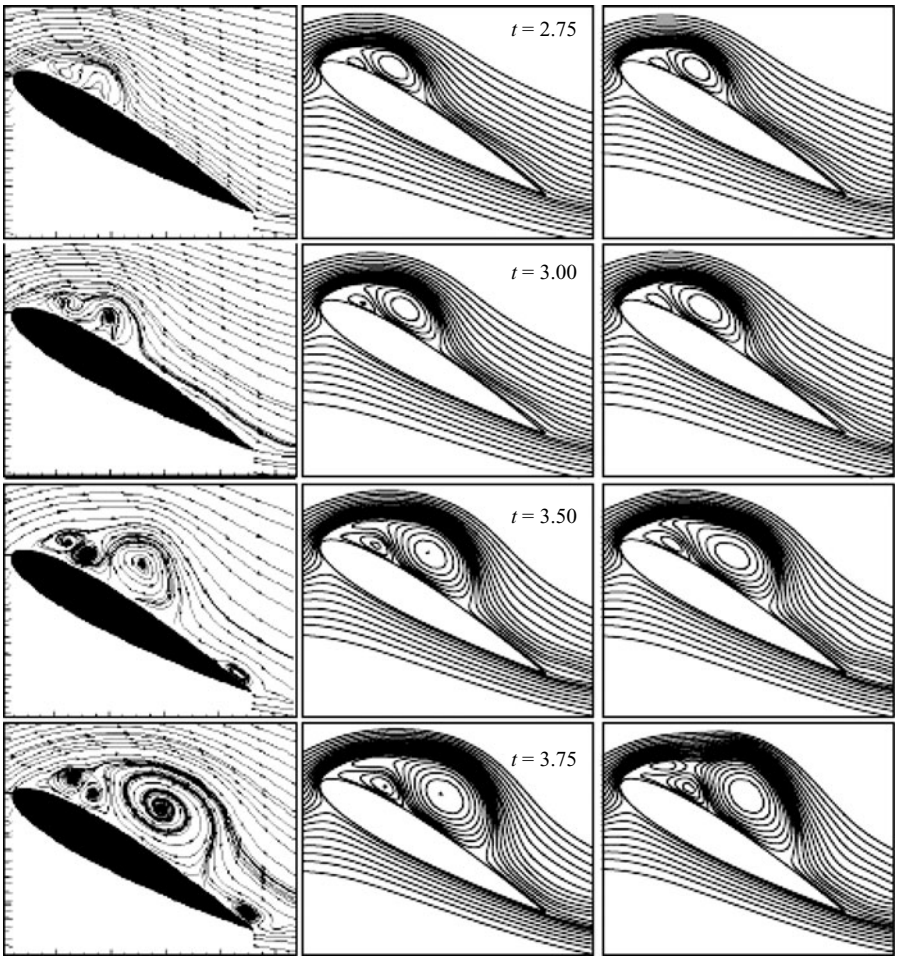

FIGURE 8. Flow field of an accelerating flow over a NACA 0015 aerofoil for A33 acceleration case at $Re = 7968$ and $\alpha = 30°$. Comparison of experimental results (left) with computed streamline contours calculated with the data of figure 7(*b*) (middle) and with the data of figure 7(*c*) (right) from $t = 0.5$ to $t = 3.75$.

surface of the aerofoil in the experimental results. In contrast, this feature of the separation bubble is clearly seen in figure 10(*b*). As discussed in Nair & Sengupta (1997*b*, 1998), the computational results of figure 10(*c*) resemble a case computed by the present method using the free-stream speed established by an impulsive start condition. The distorted primary bubble with flattened top is captured by following the correct free-stream speed variation, thus emphasizing the need to correctly specify the start-up process.

To show this sensitivity to the start-up process, we have performed another calculation (Case C) where the final free-stream speed is achieved following a ramp start, i.e. the flow starts from zero velocity and reaches the terminal speed at $t = \tau$. Computed streamlines are shown in figure 10(*d*), and it is evident that the separation bubble for this case is under-developed compared to that in figure 10(*b*). Also, the secondary and tertiary vortices are either significantly weaker or not visible, while the primary bubble covers and extends beyond the top surface. The reason for the

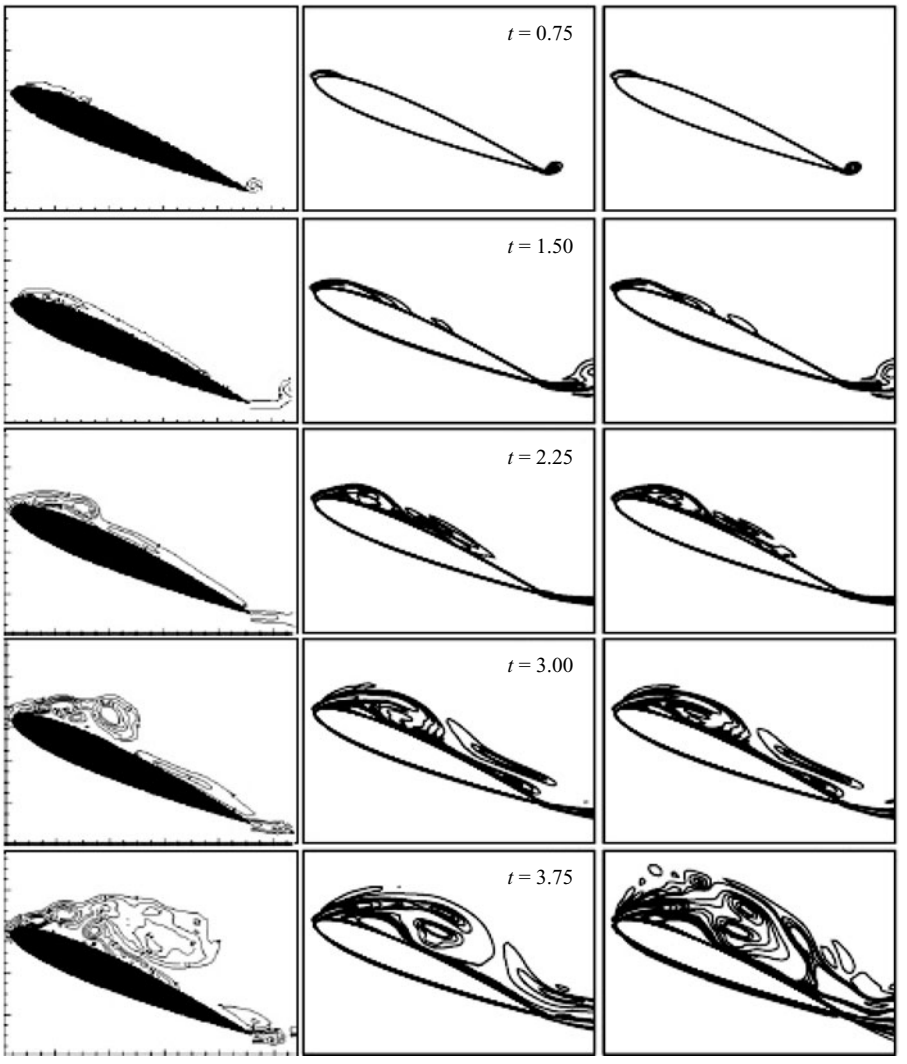

FIGURE 9. Vorticity field of an accelerating flow over a NACA 0015 aerofoil for A33 acceleration case at $Re = 7968$ and $\alpha = 30°$. Comparison of experimental results (left) with computed vorticity contours calculated with the data of figure 7(*b*) (middle) and with the data of figure 7(*c*) (right).

differences between this and Case B is the duration over which the acceleration is applied. It has already been noted with respect to the experimental results in figures 4 and 5 that the acceleration effects are more significant when it is applied over longer duration and are not strongly dependent on the level of acceleration. For Case C, the acceleration is applied over a shorter duration (τ) than Case B (as shown in figure 7*a*), which is roughly three times longer than for Case C. In Nair & Sengupta (1997*b*), it was noted that the most significant parameter is the first-vortex formation time. If the acceleration time is lower than this, then one can consider the flow to be impulsively started, otherwise detailed flow start-up has to be considered, as seen here. It is for this reason that the computed flows past bluff bodies for impulsive start match well with experimental results when the flow in the experimental facility is established quickly,

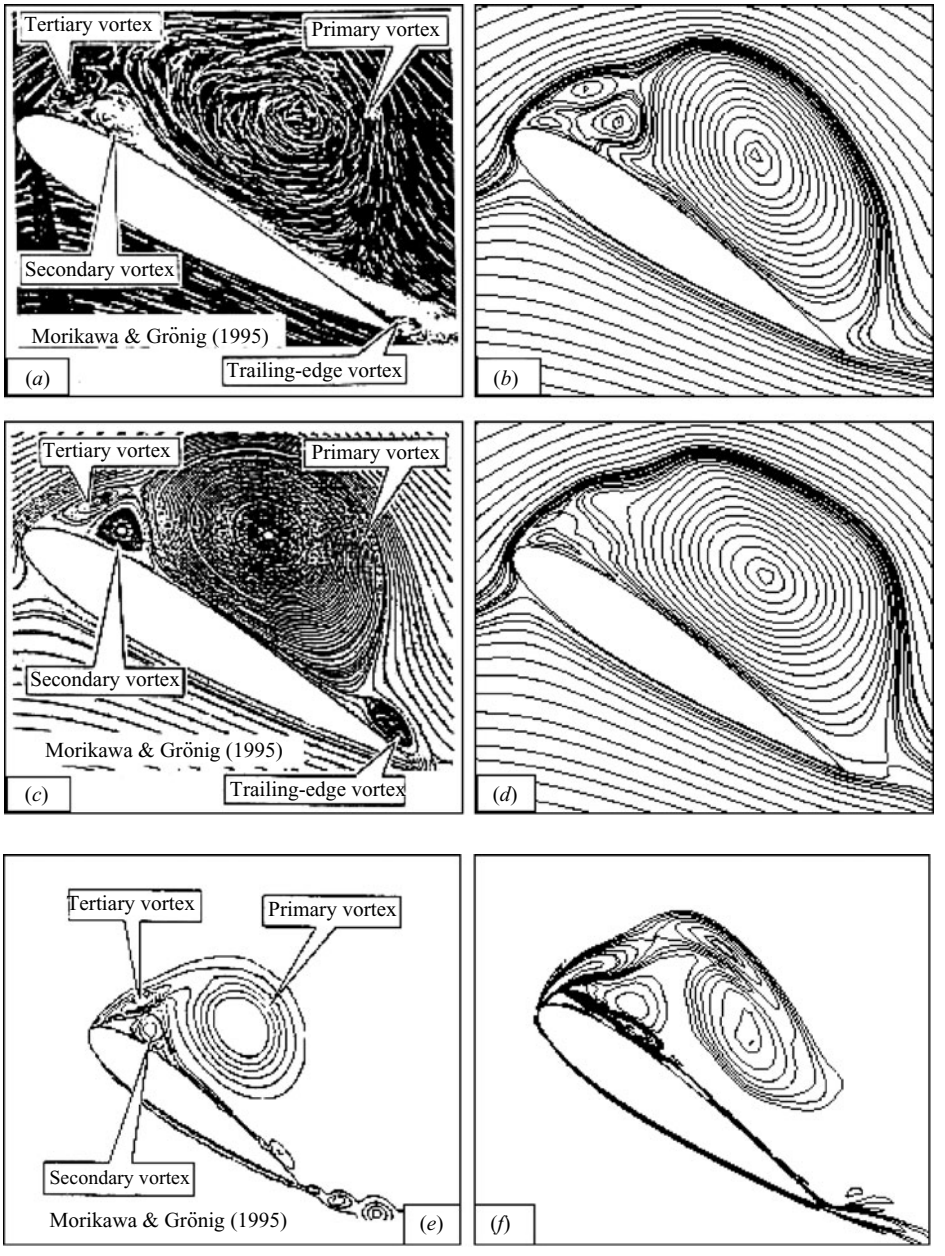

FIGURE 10. Comparison of (*a*) experimental visualization of Morikawa & Grönig (1995) with (*b*) present computational instantaneous streamlines for the acceleration following equation (1.1). (*c*) Computed results by Morikawa & Grönig (1995) and (*d*) present computed streamline following ramp start. (Note: All the results are shown for $t = 2.903$, and the computations for (*b*) and (*d*) are performed based on the velocity record shown in figure 7(*a*)). Computational vorticity contours by Morikawa & Grönig compared to (*f*) the present computational results for the case shown in (*b*).

before the formation of the first vortex. This was verified in Nair, Sengupta & Chauhan (1998) for flow past a rotating cylinder. Vorticity contours for Case B are shown in figures 10(*e*) and 10(*f*) at the same time, the former as computed by

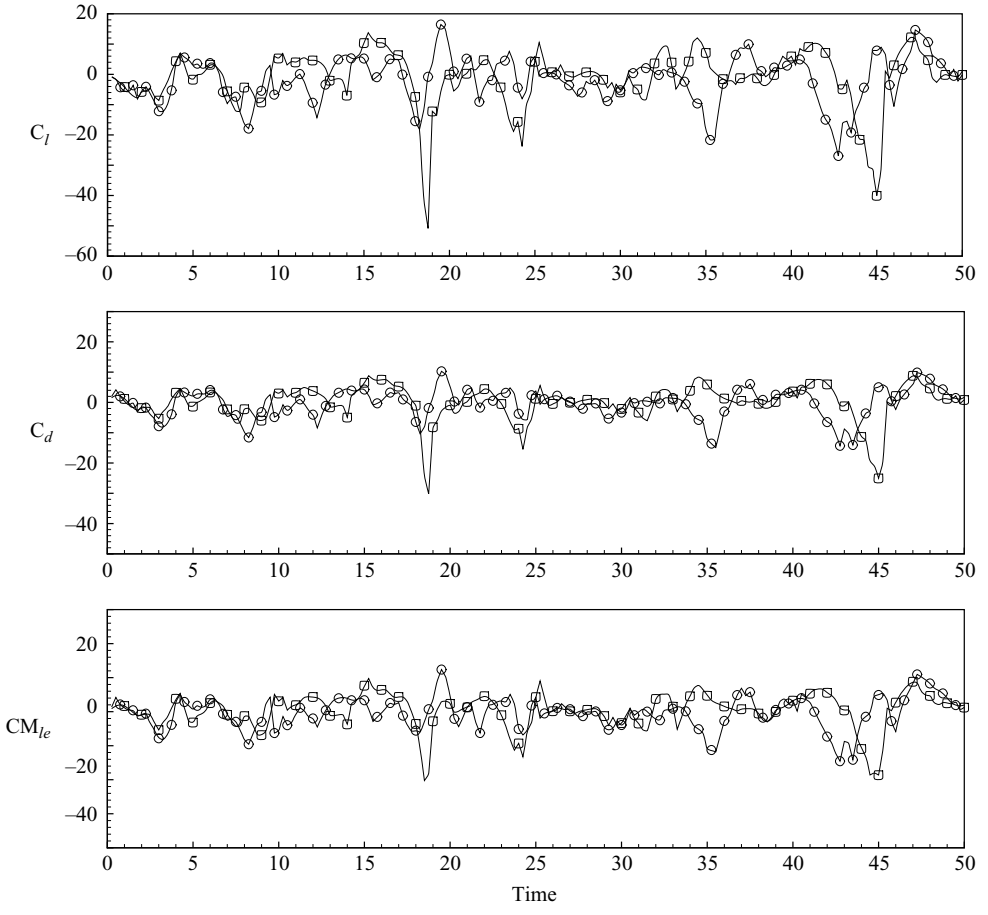

FIGURE 11. The integrated load and moment coefficients for tangent hyperbolic (square) and ramp start (circle) as shown in figure 7(*a*).

Morikawa & Grönig (1995) and the latter as computed here. Both the calculations use the non-inertial frame of reference. The other reason for the poor match of the computational results of Morikawa & Grönig (1995) with the experimental results could be the use of a lower-order method that filters high-wavenumber events that may have significant effects on flow evolution. While the higher-order methods capture the shear layer instabilities adequately, the same effects with lower-order methods require very high grid resolution.

Cases B and C are calculated for longer duration in order to study the loads and moment acting on the aerofoil. This requires solving the pressure Poisson equation (3.8) over the whole domain. Calculated lift, drag and pitching moment coefficients are shown in figure 11 up to $t = 50$. Although the flow may not remain two-dimensional over long times, these results provide a qualitative picture and demonstrate that the two strategies of flow start-up yield different time-averaged lift and moment coefficients. Large jumps in the load and pitching moment coefficients displayed in figure 11 are caused by the formation, growth and shedding of dynamic stall vortices over the top surface.

A comparison of the two different start-up accelerations for the flow shows the load to be different due to different unsteadiness caused by flow separation. Even though

the loads for the two cases do not follow the same curve as in Lugt & Haussling (1978) and Gendrich *et al.* (1995), they have the same order of magnitude and follow similar trends. In Lugt & Haussling (1978) and Gendrich *et al.* (1995), acceleration was completed by time $t = 0.25$, which is before the formation of the first leading-edge bubble. Sarpkaya (1991) also obtained a similar trend for drag, following the same curve for the case where the acceleration parameter A_p was greater than 0.27. For all other cases where $A_p < 0.27$, the drag reached a quasi-steady state. In contrast, the leading-edge vortices observed here are already formed before the acceleration phase is completed and the detailed load variation depends on the formation time of the first vortex and subsequent instabilities of the separated shear layer.

In both cases, there is little interaction between vortices shed from leading and trailing edges at this Reynolds number and the angle of attack of the aerofoil, as also noted in Huang & Lin (1995). The vortex shedding is predominantly from the leading edge only, and is different from the Kármán vortex streets behind bluff bodies. For the lower Reynolds number case shown in figure 8, the shear layer separated from the leading edge does not shed clearly and interacts with the separated shear layer from the trailing edge, causing slow time variation of physical variables in the wake. Such an interacting leading-edge laminar separation bubble was also noted by Lin & Pauley (1996), Zaman *et al.* (1989) and Sugavanam & Wu (1982). They concluded that the low-frequency oscillation over the aerofoil is due to the vortex shedding from laminar separation bubbles.

Similarly, comparing the present computations for flow past an aerofoil to that for ellipses in Nair & Sengupta (1997*a*), it is noticed that the leading-edge stagnation point does not move for the aerofoil at post-stall angles of attack of 30°. Also, the rear stagnation point is always near the trailing edge except when *alleyways* are formed. This is due to the presence of the sharp trailing edge and the resultant interactions of vortices in the wake are relatively weaker for aerofoils than to ellipses.

4.3. *Case D*

This case corresponds to the experimental results reported in Freymuth (1985) for the uniform acceleration case at significantly higher angles of attack, while the maximum Reynolds number is fixed at 5200. This particular case of uniform acceleration has a higher acceleration level, with τ much larger than for the previous cases. Of all the experimental cases in Freymuth (1985), 60° and 90° angle of attack cases are computed because of the stronger vortical structures seen in the experimental visualizations, and such cases have not been computed before. For the flow visualization in Freymuth (1985), liquid titanium tetrachloride ($TiCl_4$) is applied on the aerofoil surface, and the 'smoke' produced by the evaporation of the injected liquid is accumulated in the low-velocity recirculation zone. It is therefore difficult to give a proper interpretation of the visualization pictures. These are in a strict sense not streaklines as the amount of liquid injected is so large that the 'smoke' does not emanate from a single point. The visualization pictures reveal a combination of high-stress and low-convection pockets. Thus, the pictures can be compared qualitatively with vorticity and pressure contours. Also, due to the slightly reflective surface of the aerofoil, a mirror image of the detected structures is also captured in the visualization pictures.

4.3.1. *Cases of* $\alpha = 60°$ *and* $90°$ *for* $Re = 5200$

Here, the Reynolds number is in the same range as the experiments of Case A. But the angle of attack is increased so that the vortices shed from the leading and trailing edges are more pronounced. Also, the acceleration level is $2.4\,\mathrm{m\,s^{-2}}$,

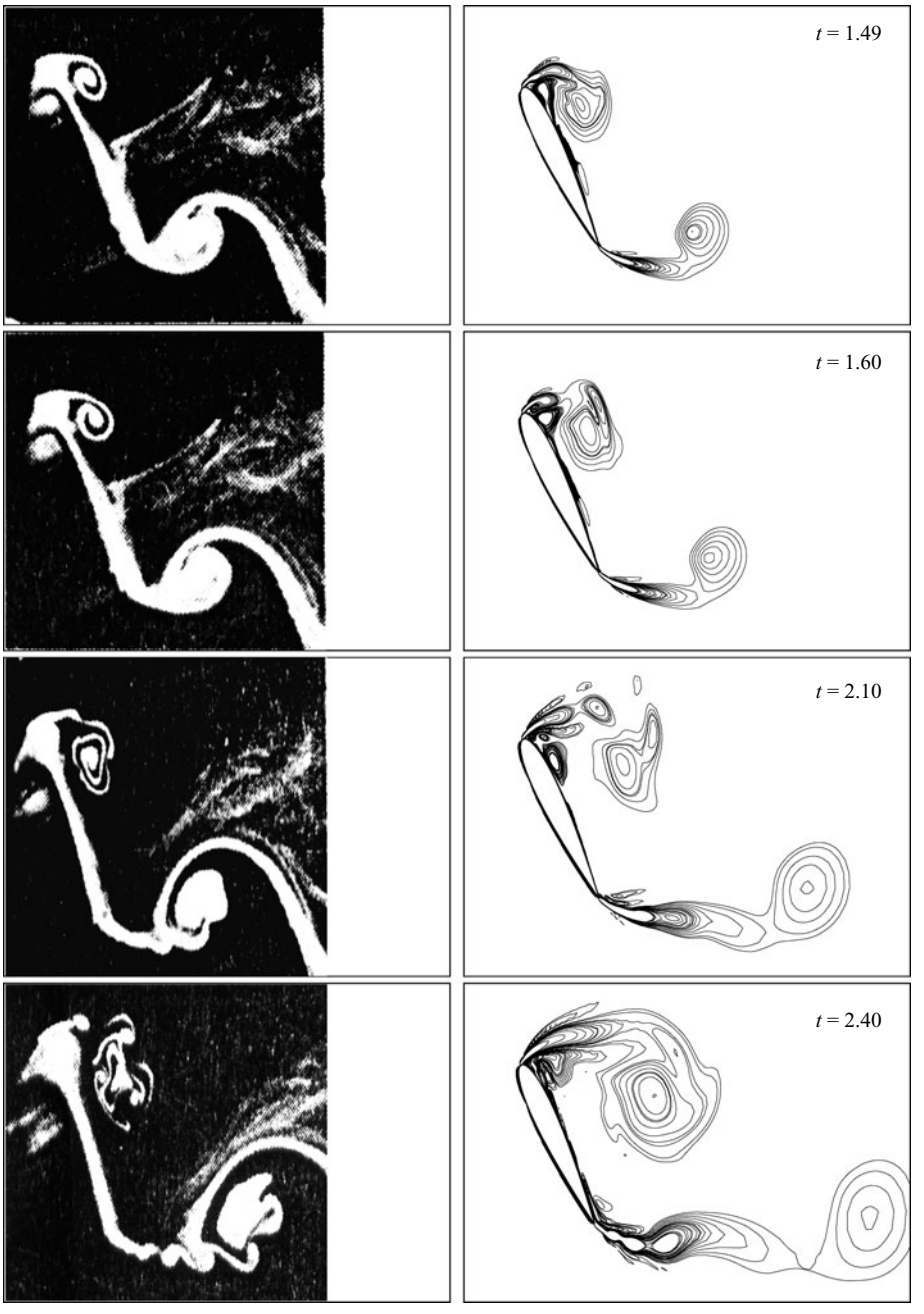

FIGURE 12. For caption see facing page.

which is orders of magnitude higher than in our experimental results shown in figures 4 and 5. Computed vorticity contours at discrete times are compared with the flow visualization performed in Freymuth (1985) (see figure 12 for $\alpha = 60^\circ$). The match between the experiment and computation is striking for all the frames up to $t = 3.29$, at least for the vortices that emanate from the leading edge of the aerofoil. The agreement between the experiment and computations is less

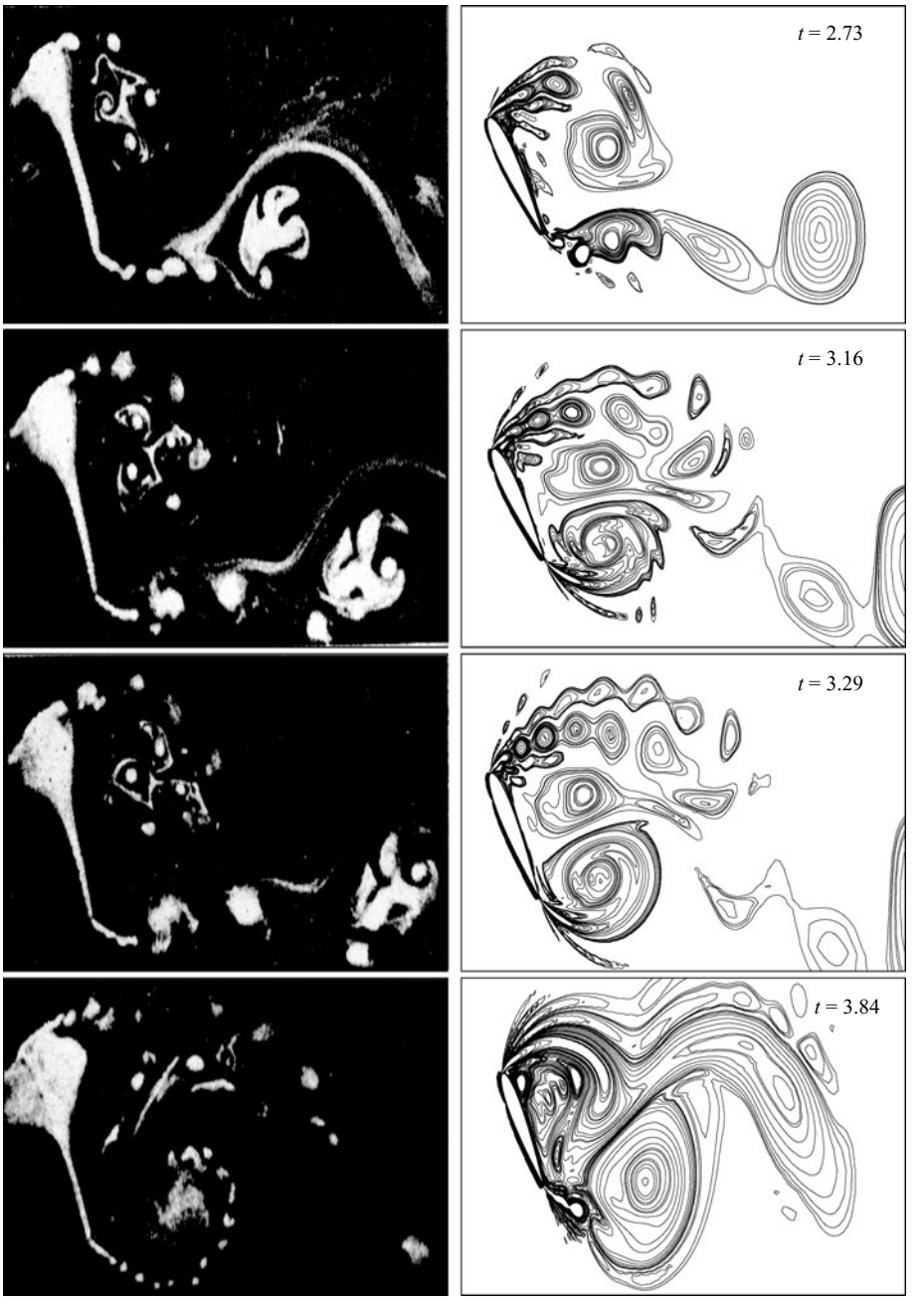

FIGURE 12. Comparison of present vorticity contours (right) with visualization pictures (left) from Freymuth (1985) for $Re = 5200$ and $\alpha = 60^\circ$ and time increasing from $t = 1.49$ to $t = 3.84$.

satisfactory for the vortical structures released from the trailing edge of the aerofoil. While two-dimensional calculations are capable of capturing vortices created by the combined action of local flow acceleration followed by rapid deceleration near the leading edge, vortices emerging from the trailing edge show a tendency of merging in a two-dimensional simulation, as noted in Lesieur & Metais (1996). This so-called backscatter problem was discussed in Mathaeus *et al.* (1991) and Brachet *et al.*

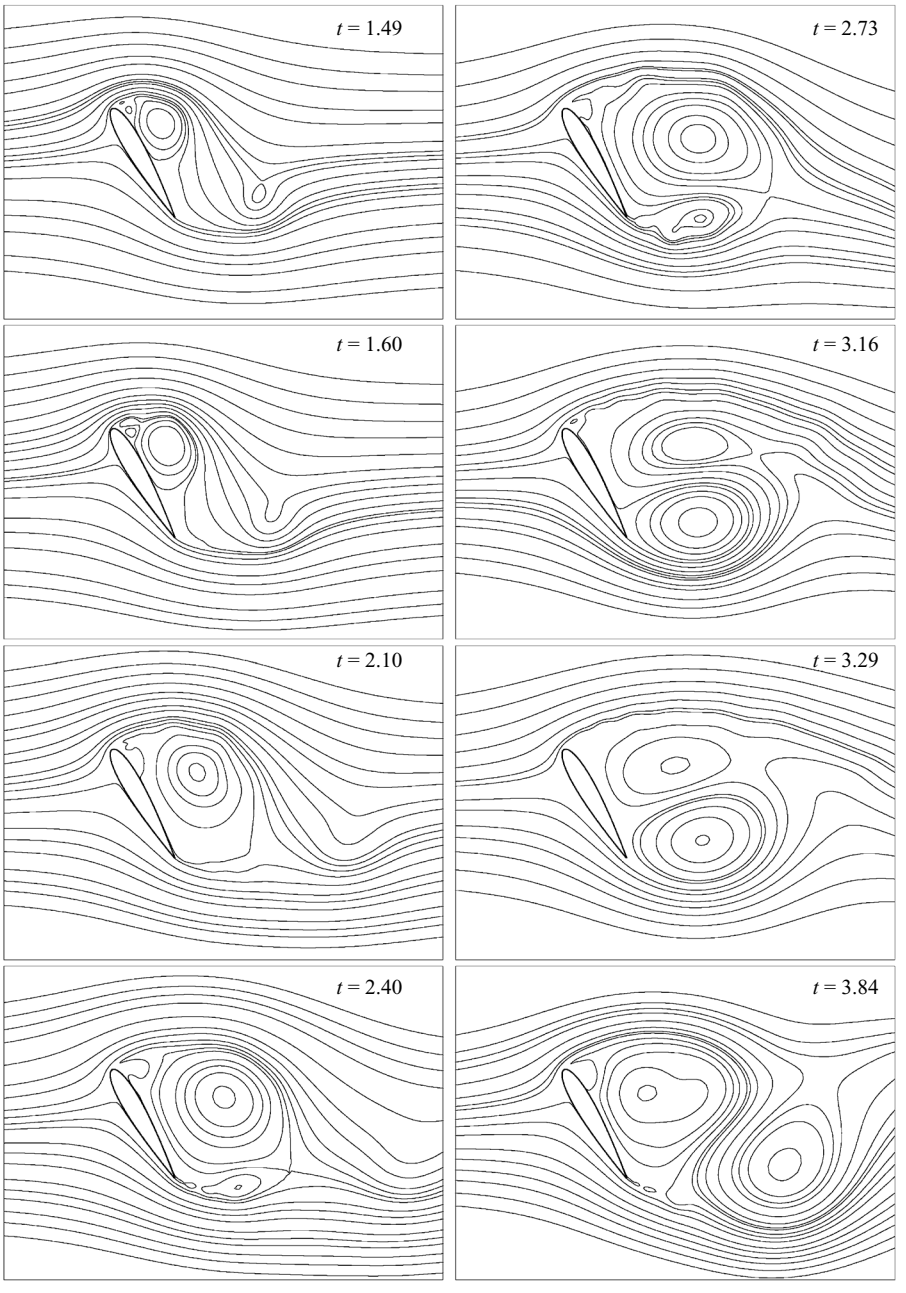

FIGURE 13. Streamline contours at different times for $Re = 5200$ and $\alpha = 60^\circ$ for the case in figure 12.

(1994). It appears that in an actual flow, three-dimensionality plays a major role near the trailing edge, which the present two-dimensional computations cannot capture.

In figure 13, the streamline contours are shown plotted at selected time instants for the $\alpha = 60^\circ$ case. For the early time up to $t = 2.10$, the bubble created on the top surface near the leading edge keeps growing, while a secondary vortex is always positioned near the leading edge. Subsequently, a trailing-edge bubble appears as can

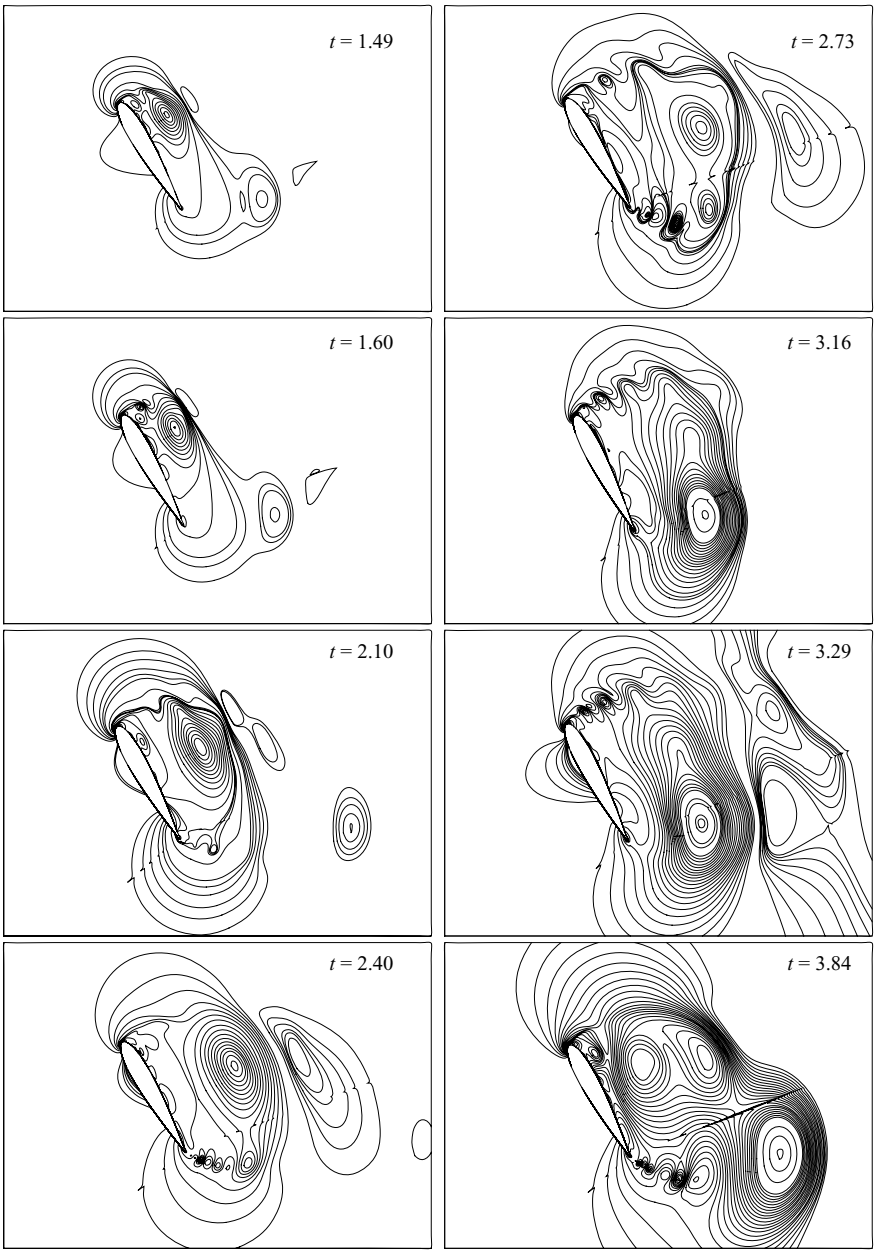

FIGURE 14. Total pressure contours at different times for $Re = 5200$ and $\alpha = 60^\circ$ for the case in figure 12.

be seen in the frame at $t = 2.40$. This bubble continues to grow, while the top bubble continues to reduce in size. Soon after $t = 3.29$, the trailing-edge bubble is released as can be seen at $t = 3.84$. Thereafter, the primary bubble starts to grow again.

It was noted earlier that the flow visualization pictures display structures that can be compared to vorticity and pressure contours. For this reason, total pressure contours are plotted in figure 14 at selective time instants for the case of $\alpha = 60^\circ$. At $t = 1.49$ and $t = 1.60$, the dye blobs are seen at those locations where the pressure

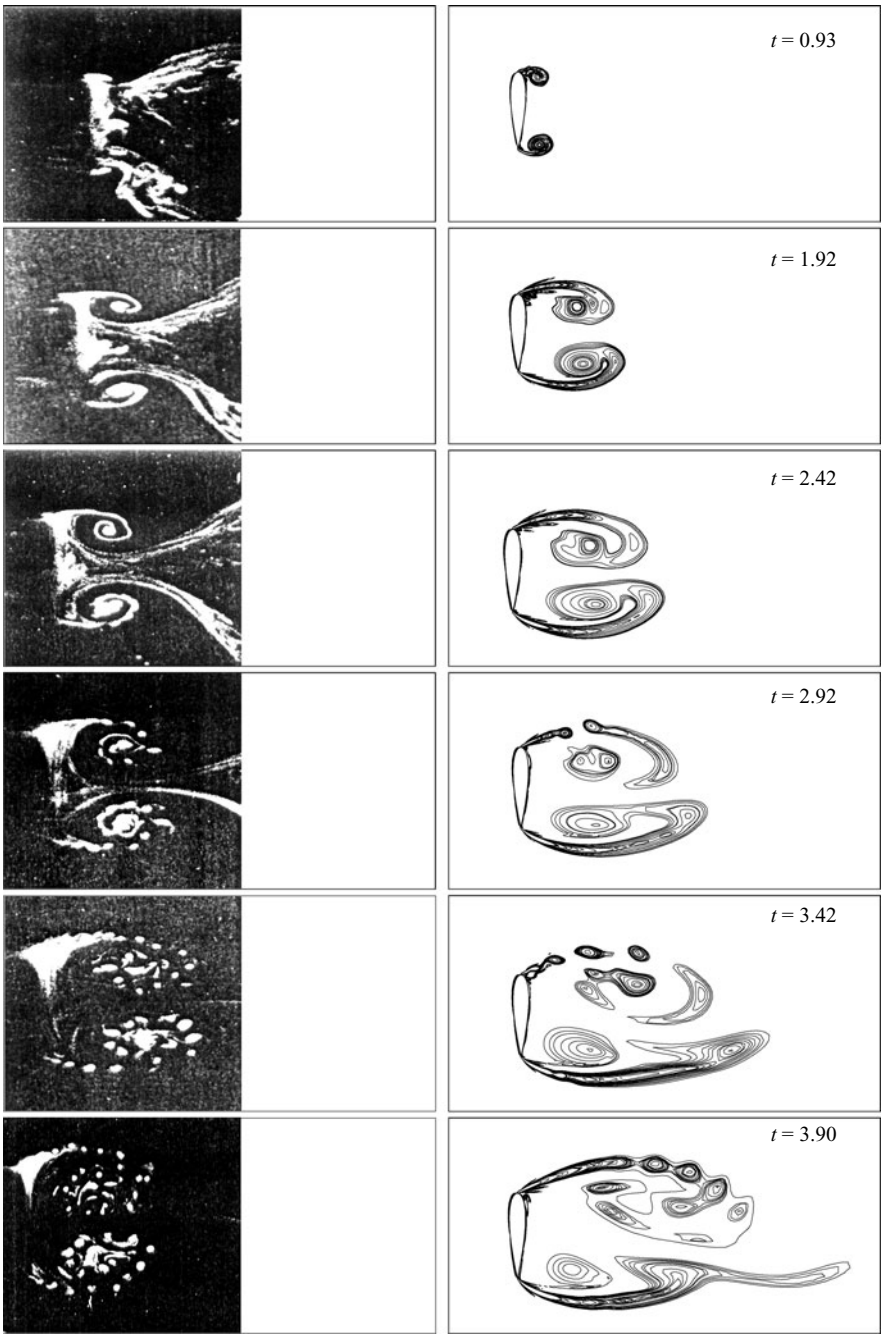

FIGURE 15. Comparison of the present vorticity contours (right) with visualization pictures (left) from Freymuth (1985) for $Re = 5200$ and $\alpha = 90^\circ$.

contours show major centres. Such a correspondence is not seen readily at later times although a chain of vortices created by Kelvin–Helmholtz instability is seen to emerge from the leading edge.

Next, we have computed another case given in Freymuth (1985) for an angle of attack of 90° for the same Reynolds number. The computational results are compared to the experimental results in figure 15 at selected times. This case resembles that of

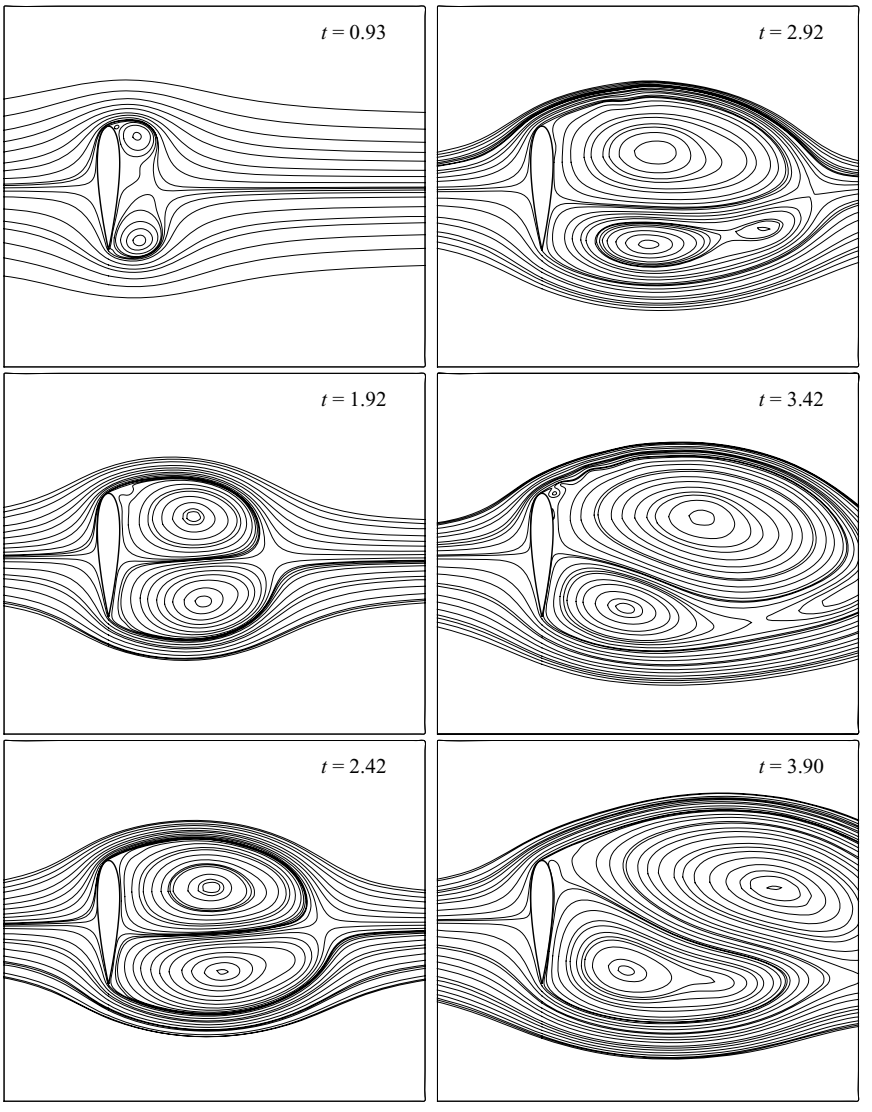

FIGURE 16. Streamline contours at different times for $Re = 5200$ and $\alpha = 90^\circ$ for the case in figure 15.

a normal flat plate, except that the vortices shed from the leading and trailing-edges are dissimilar due to differences in shape and curvature of the leading and trailing edges. Similar to the case shown in figure 12 for $\alpha = 60^\circ$, the bubbles shed from the top (clockwise vortices) also suffer Kelvin–Helmholtz instability and a train of smaller vortices formed are captured quite accurately in the computation for all the time frames shown. For similar reasons as cited for $\alpha = 60^\circ$ case, the anticlockwise vortices shed from the trailing edge show backscatter (vortex merger) while convecting downstream, and the agreement with experimental results for the vortical structures is less than satisfactory. In figure 16, the streamline contours are shown at the same time instants as in figure 15. There are dissimilar bubbles downstream of the aerofoil, with a larger vortex on the trailing-edge side than on the leading-edge side. Both these vortices keep growing with time till $t = 1.92$ when the lower bubble is marginally bigger than the upper one. One can also see an *alleyway* forming around

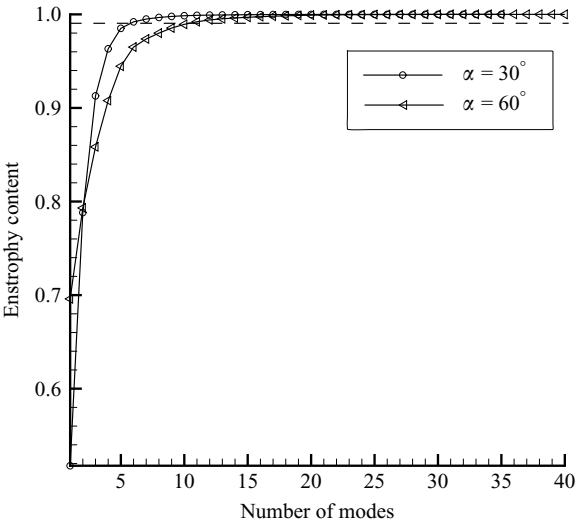

FIGURE 17. Sum of a specific number of eigenvalues divided by their total sum, showing enstrophy content. The dashed line marks 99 % enstrophy level.

the bubble on the upper side of the aerofoil. Despite this, the top bubble is seen to grow more rapidly at $t = 2.42$ than the lower bubble. However, at $t = 2.92$, the top bubble becomes bigger, while the vortex in the lower bubble starts to split into two. At $t = 3.42$, the upper bubble grows further and the lower bubble has split into two, with the rear stagnation point located at mid-chord on the top surface. In the last frame, at $t = 3.90$, the top bubble detaches from the aerofoil causing the rear stagnation point to move towards the leading edge on the top surface.

5. Proper orthogonal decomposition and disturbance energy creation

Here, we perform proper orthogonal decomposition (POD) of the vorticity data for the two cases shown in figures 9 (for $Re = 7968$ and $\alpha = 30°$) and 12 (for $Re = 5200$ and $\alpha = 60°$) following the method of snapshots due to Sirovich (1987). For the former case, we have used 35 snapshots starting from $t = 0.1$ up to $t = 3.5$ for the disturbance vorticity; for the latter case, 40 snapshots have been used from $t = 0.1$ to 4.0. The disturbance vorticity is calculated by subtracting the mean over this time period from the instantaneous data. The details of the exact method are also given in Sengupta & Dipankar (2005) and are not repeated here. Vortical structures obtained from the POD analysis provide a statistical fit of the ensemble during the time period, by minimizing the projection error of the data onto a set of deterministic eigenvectors. The eigenvectors (X) are obtained from the linear algebraic equation: $RX = \lambda X$, with R the covariance matrix whose elements are formed from the disturbance vorticity ($\omega'(x_i, t_m)$) as: $R_{ij} = 1/M \sum_{m=1}^{M} \omega'(x_i, t_m)\omega'(x_j, t_m)$, with $i, j = 1, 2, \ldots . N$ defined over all collocation points totalling to N. These complete eigenvectors correspond to the eigenvalues λ that define the probability of their occurrence and their sum gives the total enstrophy of the system.

In figure 17, the cumulative enstrophy content, as given by the sum of a specific number of eigenvalues divided by their total sum, is plotted along the ordinate and the number of modes along the abscissa; a dotted line indicates 99 % level of enstrophy.

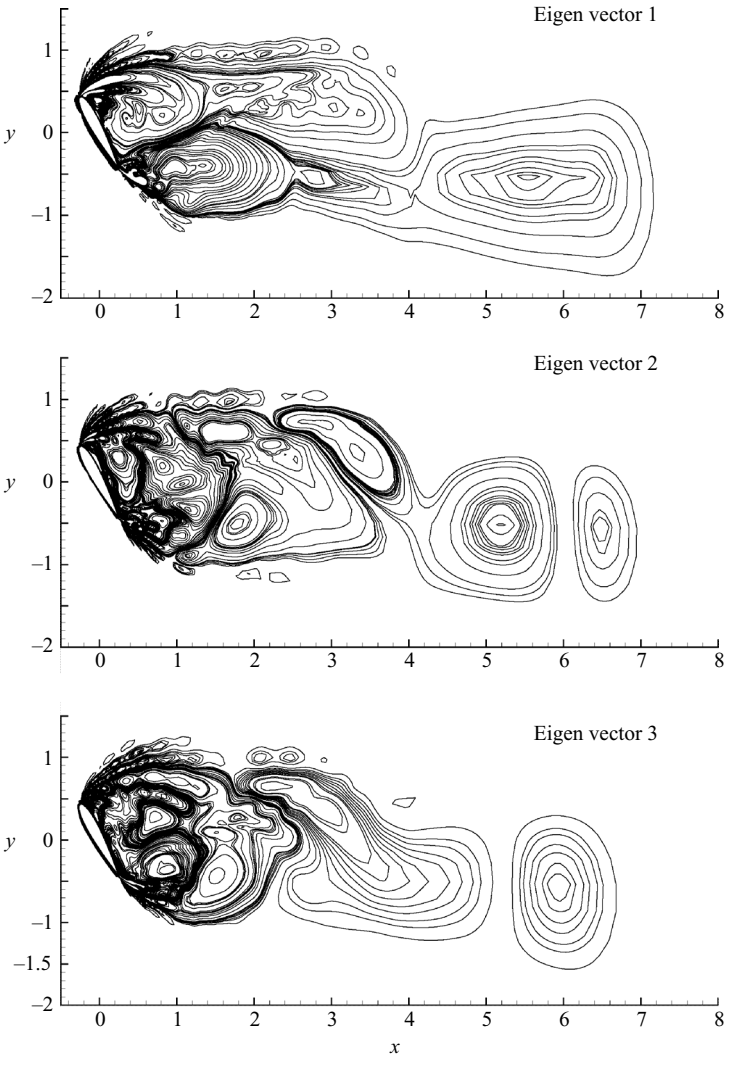

FIGURE 18. The first three eigenvectors of disturbunce vorticity during the time range 0.1 to 4.0 for $Re = 5200$ and $\alpha = 60^\circ$ case.

It is seen that for $\alpha = 60^\circ$, 11 modes are required to represent this level, while for $\alpha = 30^\circ$, only five modes are adequate to represent 99 % of the total enstrophy.

In figure 18, only the first three eigenvectors are shown for the case of $Re = 5200$ and $\alpha = 60^\circ$. The first eigenvector shows a staggered, near-symmetric vortical structure in the near wake. Additionally, a chain of small vortices is seen above the top vortical structure. Since the first mode itself accounts for 70 % of total enstrophy, the primacy of the Kelvin–Helmholtz (KH) instability is clear here. However, there are no such instabilities seen in the lower half, near the trailing edge. The second eigenvector accounts for smaller scale vortices in the near wake, while larger scale vortices formed by merger are noted further downstream for all the eigenvectors. The second mode accounts for nearly 6 %, while the third mode accounts for another 5 % of the total enstrophy. Also, in the higher modes, the signature of KH instability is seen to be smaller.

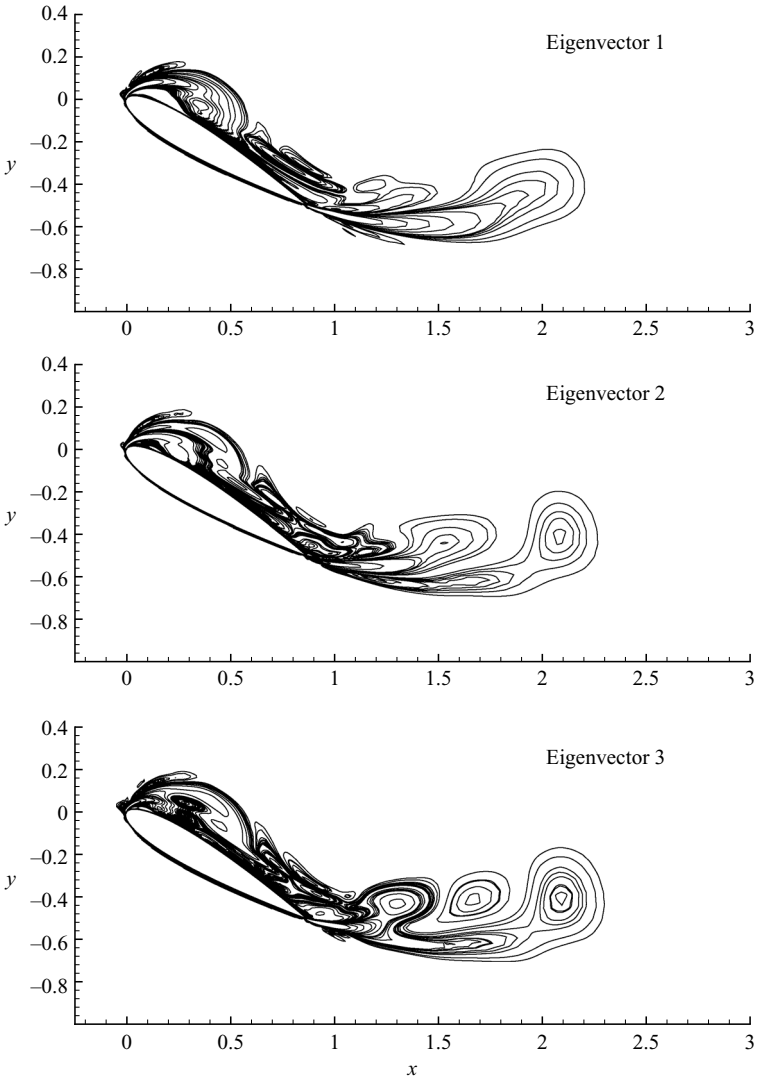

FIGURE 19. The first three eigenvectors of disturbunce vorticity during the time range 0.1 to 3.5 for $Re = 7968$ and $\alpha = 30^\circ$ case.

In figure 19, the first three eigenvectors are shown for the case of $Re = 7968$ and $\alpha = 30^\circ$. From figure 17, one notices that the first mode accounts for about 50 % of the enstrophy; the second mode contributes another 30 % of the enstrophy and the third mode takes the cumulative enstrophy content up to 92 %. None of the eigenvectors in this case displays any traces of KH instability. Multiple vortical structures are bigger, caused by laminar separation only. This is true for all three modes. The adherence of vortical structures shed from the leading edge to the top surface causes convected vortices to interact with the vortices shed from the trailing edge of the aerofoil.

Finally, we investigate the formation of a separation bubble by a diagnostic tool used in Sengupta & Dipankar (2005). If we define the total mechanical energy by $E = p/\rho + V^2/2$, then it is shown in Sengupta & Dipankar (2005, and in other references contained therein), that the instantaneous distribution of disturbance energy

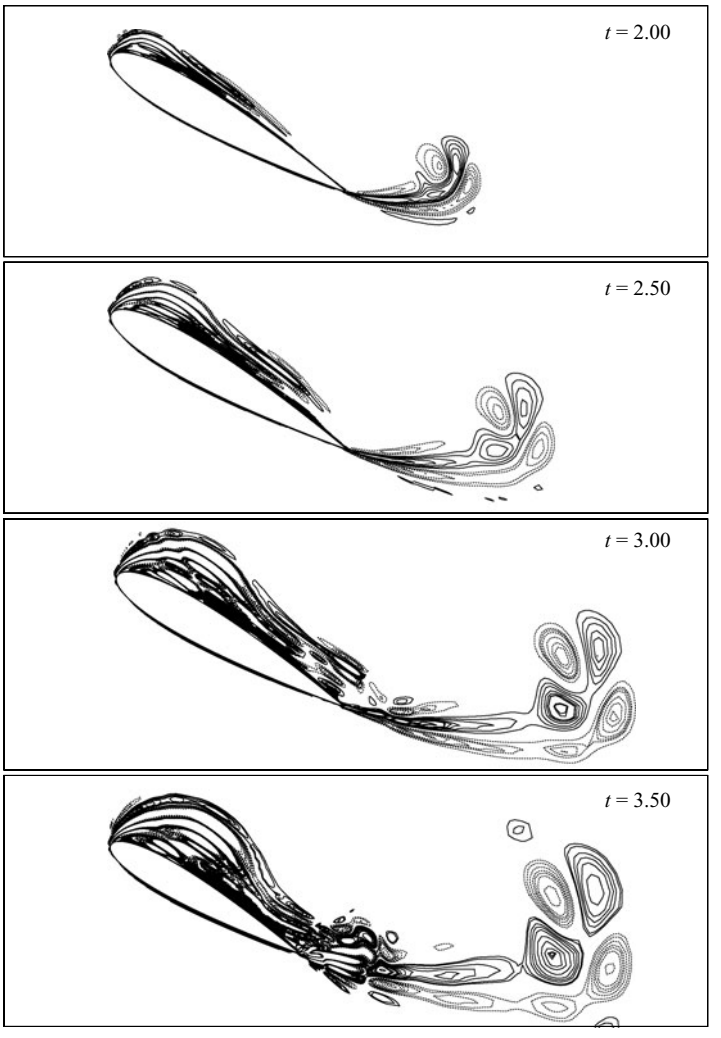

FIGURE 20. Right-hand side of the disturbance energy equation (5.1) for $Re = 7968$ and $\alpha = 30^\circ$ for the times indicated.

(E_d) is given by

$$\nabla^2 E_d = 2\boldsymbol{\omega}_m \cdot \boldsymbol{\omega}_d + \boldsymbol{\omega}_d \cdot \boldsymbol{\omega}_d - \boldsymbol{V}_m \cdot \nabla \times \boldsymbol{\omega}_d - \boldsymbol{V}_d \cdot \nabla \times \boldsymbol{\omega}_m - \boldsymbol{V}_d \cdot \nabla \times \boldsymbol{\omega}_d \qquad (5.1)$$

where the subscript m refers to a chosen equilibrium state and the subscript d refers to an appropriate disturbance flow. Here, if we denote $\omega_m = \omega(t)$ and $\omega_d = \omega(t + N\Delta t) - \omega(t)$, where $N\Delta t$ is a predetermined time interval, then the right-hand side of the above Poisson equation provides the forcing that will dictate the instantaneous distribution of E_d. In the present case, we have used $N\Delta t = 10^{-3}$, such that (5.1) gives an almost instantaneous description of the disturbance energy creation. It has been shown in Sengupta & Dipankar (2005) that the vortices are formed depending on the sign of the right-hand side of (5.1), and that in turn indicates an *energy source* (when it is negative) or *energy sink* (when it is positive).

In figure 20, contours of the right-hand side are plotted for the case of figure 9. The similarity between these and the vorticity plots of figure 9 indicates that this

type of vortex-dominated flow is dictated by the mechanism of disturbance energy creation given by (5.1) that is adequate when using the solution of two-dimensional Navier–Stokes equation.

6. Summary and concluding remarks

Incompressible accelerated flow past an aerofoil is studied here experimentally and computationally at low Reynolds numbers and high angles of attack. Different types of acceleration are considered, for which the major effects seen are related to unsteady flow separation and their instabilities.

Specifically, a constant acceleration case and another case where the free-stream speed reaches its final value via a non-uniform acceleration following a tangent hyperbolic variation are studied. For both cases, limited experimental results are available and additional experiments were conducted for NACA 0015 aerofoil experiencing uniform acceleration for $Re = 7968$ and an angle of attack of $\alpha = 30^\circ$. The experiments have been performed in a piston-driven closed-circuit water tunnel. Experimentally obtained velocity and vorticity fields through PIV measurements have been presented in figures 4 and 5 for three different levels of accelerations in the piston-driven water tunnel. It is noted from these results that the unsteady separation leading to bubble formation depends more on the duration of applied acceleration than on the severity of the acceleration.

Computational results have been presented for different cases using an accurate method to solve time-dependent two-dimensional Navier–Stokes equations in stream function–vorticity formulation. This methodology has been well-tested on many problems of unsteady flows undergoing transition. The case of uniform acceleration that displayed maximum unsteady separation in the experiments performed have been studied computationally and the results compared in figures 8 and 9. We have also measured the flow velocity in the tunnel and noted some variations with the piston velocity as shown in figures 7(*b*) and 7(*c*). The reason for the difference is traced to the fluid loading in the tunnel causing a small deformation of the square section. Despite the small variations between these two cases, we note only small differences and found that the simulations performed with actual measured velocity match better with the experimental data. Since the measured velocity was low-pass filtered, the comparison should improve further, if the higher frequency components of the actual velocity are also included.

To study the effects of different types of accelerations, experimental results of Morikawa & Grönig (1995) were simulated for $Re = 35\,000$ and $\alpha = 30^\circ$, when the free-stream speed varies according to equation (1.1). Comparison between the experimental results and computations shows very good agreement (see figure 10) when the computations are performed with the actual time variation of the free stream. Our computed results show even better agreement with the experiment than that provided in Morikawa & Grönig (1995) by a finite volume formulation. This establishes the superiority of the formulation and methods employed in the present study.

Effects of higher angles of attack have been investigated by computing some cases reported in Freymuth (1985) for $Re = 5200$, with the flow experiencing acceleration levels eighty times higher than in our experiments. The cases computed here are for $\alpha = 60^\circ$ and 90° and the comparisons are shown in figures 12, 13 and 15. Displayed results in figures 12 to 16 show the central importance of Kelvin–Helmholtz (KH) type instability of the separated shear layer at these high angles of attack. It is

also noted that the agreement between the experiments and the computations is particularly good for the top part of the flow that shows shedding of clockwise vortices that undergo KH instability to create smaller vortices. The agreement is less satisfactory for the weaker bubble created at the trailing edge. Calculations reveal backscatter or merger of smaller vortices near the trailing edge, a well-known feature of two-dimensional simulations. This leads us to believe that the flow is affected more by three-dimensionality near the trailing edge than the leading edge. This can explain computational observations.

The lack of small-scale vortices formed by KH instability for lower angles of attack is also supported by the POD results shown in figures 17 to 19, for the cases whose vorticity contours are shown in figures 9 and 12. It is noted that for the lower angle of attack ($\alpha = 30^\circ$), there is no evidence of KH instability, and the bubble formed near the leading edge slowly convects down the top surface and interact with vortices formed at the trailing edge. The first eigenvector accounts for nearly 50 % of the total enstrophy and overall only five modes are necessary to represent 99 % of total enstrophy. For the $\alpha = 60^\circ$ case, first mode accounts for 70 % of total enstrophy and 11 modes are needed to describe 99 % of total enstrophy. It is noted that the vortical structures in the near wake are elongated in the streamwise direction for the low angle of attack case, while for the higher angle of attack, the structures occupy the full base region. Finally, vortex creation by the disturbance energy description of Sengupta & Dipankar (2005) is analysed for a case tested and computed here. Close correspondence of vortex location with the location of the major disturbance sources and sinks establishes the utility of (5.1) as a diagnostic tool to predict flow separation.

REFERENCES

Badr, H. M., Dennis, S. C. R. & Kocabiyik, S. 1996 Symmetrical flow past an accelerated circular cylinder. *J. Fluid Mech.* **308**, 97–110.

Brachet, M., Meneguzzi, M., Politano, H. & Sulem, P. 1988 The dynamics of freely decaying two-dimensional turbulence. *J. Fluid Mech.* **194**, 333–349.

Brendel, M. & Mueller, T. J. 1988 Boundary-layer measurements on an airfoil at low Reynolds numbers. *J. Aircraft* **25**, 612–617.

Carr, L. W. & Chandrasekhara, M. S. 1996 Compressibility effects on dynamic stall. *Prog. Aero. Sci.* **32**, 523–573.

Choudhuri, P. G. & Knight, D. D. 1996 Effects of compressibility, pitch rate, and Reynolds number on unsteady incipient leading-edge boundary layer separation over a pitching aerofoil. *J. Fluid Mech.* **308**, 195–217.

Collins, W. M. & Dennis, S. C. R. 1974 Symmetrical flow past a uniformly accelerated circular cylinder. *J. Fluid Mech.* **65**, 461–480.

Currier, J. F. & Fung, K. Y. 1992 Analysis of the onset of dynamic stall. *AIAA J.* **30**, 2469–2477.

Freymuth, P. 1985 The vortex patterns of dynamic separation: a parametric and comparative study. *Prog. Aero. Sci.* **22**, 161–208.

Gendrich, S. C., Koochesfahani, M. M. & Visbal, M. R. 1995 Effects of initial acceleration on the flow field development around rapidly pitching airfoils. *Trans. ASME: J. Fluids Engng* **117**, 45–49.

Huang, R. F. & Lin, C. L. 1995 Vortex shedding and shear-layer instability of wing at low-Reynolds numbers. *AIAA J.* **33**, 1398–1403.

Koochesfahani, M. M. & Smiljanovski, V. 1993 Initial acceleration effects on flow evolution around airfoils pitching to high angles of attack. *AIAA J.* **31** 1529–1531.

Lesieur, M. & Metais, O. 1996 New trends in large-eddy simulations of turbulence. *Annu. Rev. Fluid Mech.* **28**, 45–82.

Lin, J. C. M. & Pauley, L. L. 1996 Low-Reynolds-number separation on an airfoil. *AIAA J.* **34**, 1570–1577.

Lugt, H. J. & Haussling, H. J. 1978 The acceleration of thin cylindrical bodies in a viscous fluid. *J. Appl. Mech.* **45**, 1–6.

Mathaeus, W. H., Stribling, W. T., Martinez, D., Oughton, S. & Montgomery, D. 1991 Selective decay and coherent vortices in two-dimensional incompressible turbulence. *Phys. Rev. Lett.* **66**, 2731–2734.

McCroskey, W. J. 1982 Unsteady airfoils. *Annu. Rev. Fluid Mech.* **24**, 285–311.

Mehta, U. B. & Lavan, Z. 1975 Starting vortex, separation bubbles and stall: a numerical study of laminar unsteady flow around an airfoil. *J. Fluid Mech.* **67**, 227–256.

Morikawa, K. & Grönig, H. 1995 Formation and structure of vortex systems around a translating and oscillating airfoil. *Z. Flugwiss. Weltraumforsch* **19**, 391–396.

Nair, M. T. 1998 Accurate numerical simulation of two-dimensional unsteady incompressible flows. PhD Thesis, Dept. Aero. Engng, Indian Institute of Technology Kanpur, India.

Nair, M. T. & Sengupta, T. K. 1997*a* Unsteady flow past elliptic cylinders. *J. Fluids Struct.* **11**, 555–595.

Nair, M. T & Sengupta, T. K. 1997*b* Accelerated incompressible flow past aerofoils. *Proc. 7th Asian Congress of Fluid Mechanics Madras, India, Dec. 1997.*

Nair, M. T. & Sengupta, T. K. 1998 Orthogonal grid generation for Navier-Stokes computations. *Intl J. Numer. Meth. Fluids* **28**, 215–224.

Nair, M. T., Sengupta, T. K. & Chauhan, U. S. 1998 Flow past rotating cylinders at high Reynolds numbers using higher order upwind scheme. *Computers Fluids* **27**(1), 47–70.

Ohmi, K., Coutanceau, M., Loc, T. P. & Dulieu, A. 1991 Further experiments on vortex formation around an oscillating and translating airfoil at large incidences. *J. Fluid Mech.* **225**, 607–630.

Perry, A. E., Chong, M. S. & Lim, T. T. 1982 The vortex shedding process behind two-dimensional bluff bodies. *J. Fluid Mech.* **116**, 77–90.

Ramiz, M. A. & Acharya, M. 1992 Detection of flow state in an unsteady separating flow. *AIAA J.* **30**, 117–123.

Rayleigh, Lord 1911 On the motion of solid bodies through viscous liquids. *Phil. Mag.* (6) **21**, 697–711.

Sarpkaya, T. 1991 Nonimpulsively started steady flow about a circular cylinder. *AIAA J.* **29**, 1283–1289.

Schlichting, H. 1979 *Boundary Layer Theory*, VII edn. McGraw Hill.

Sengupta, T. K. 2004 *Fundamentals of Computational Fluid Dynamics*. Universities Press, Hyderabad, India.

Sengupta, T. K. & Dipankar, A. 2005 Subcritical instability on the attachment-line of an infinite swept wing. *J. Fluid Mech.* **529**, 147–171.

Sengupta, T. K., Ganeriwal, G. & De, S. 2003 Analysis of central and upwind compact schemes. *J. Comput. Phys.* **192**, 677–694.

Sengupta, T. K., Vikas, V. & Johri, A. 2006 An improved method for calculating flow past flapping and hovering airfoils. *Theor. Comput. Fluid Dyn.* **19**, 417–440.

Sirovich, L. 1987 Turbulence and the dynamics of coherent structures. Parts 1-3: Coherent structures. *Q. Appl. Maths* **45**, 561–584.

Soria, J., New, T. H., Lim, T. T. & Parker, K. 2003 Multigrid CCDPIV measurements of accelerated flow past an airfoil at an angle of attack of 30°. *Expl Therm. Fluid Sci.* **27**, 667–676.

Stokes, G. G. 1851 On the effect of the internal friction of fluids on the motion of pendulums. *Trans. Camb. Phil. Soc.* **9**, 8–106.

Stuart, J. T. 1963 Unsteady boundary layers. In *Laminar Boundary Layers* (ed. L. Rosenhead). Clarendon Press.

Sugavanam, A. & Wu, J. C. 1982 Numerical study of separated turbulent flow over airfoils. *AIAA J.* **20**, 464–470.

Zaman, K. B. M. Q., McKinzie, D. J. & Rumsey, C. L. 1989 A natural low-frequency oscillation of the flow over an airfoil near stalling conditions. *J. Fluid Mech.* **202**, 403–442.